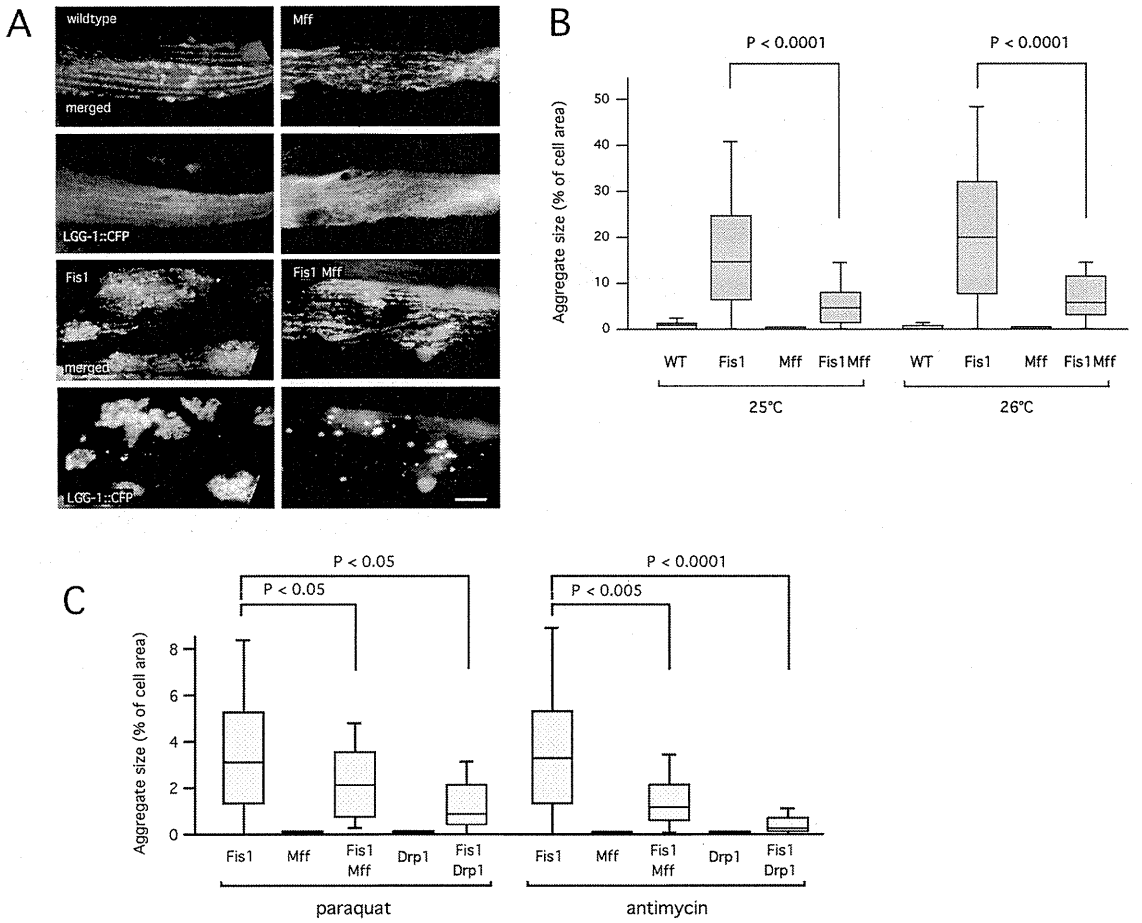

FIGURE 3: Mutations in Mff and Drp1 suppress aggregate formation. (A) The Fis1 double mutant has large aggregates when grown at 26°C. The Fis1 Mff quadruple mutant has much smaller aggregates under these conditions. Labeled as in Figure 2A. Bar, 10 µm. (B) Aggregate sizes, shown as percentages of cell surface area. Box plots represent 40 or more cells per condition (*p* values determined with unpaired Student's *t* test). Results are shown for growth at 25 and 26°C. (C) Mutations in Mff or Drp1 suppress Paraquat- and antimycin A–induced aggregate formation in Fis1 double mutants. Quantification of results is shown as in B.

26°C have no aggregates, the Fis1 mutants have large aggregates, and the quadruple mutants have much smaller aggregates (Figure 3, A and B). Similar results were obtained with Paraquat and antimycin A (Figure 3C). Inhibition of aggregate formation by a block in Mff-dependent fission shows that Mff acts upstream of the Fis1-dependent step in this process.

The order of this pathway was additionally confirmed with Drp1 overexpression and Drp1 RNAi in Fis1-mutant animals. When Drp1 is overexpressed in Fis1-mutant animals, mitochondrial fission is induced, and more and larger aggregates are formed than in the Fis1 mutant alone (Supplemental Figure S3D). In contrast, Drp1 RNAi blocks the formation of aggregates. Moreover, a *drp-1 fis-1 fis-2* triple mutant strain also had reduced number and size of aggregates when treated with Paraquat (Figure 3C). Together these results indicate that LGG-1 aggregates are formed during or after fission in Fis1 mutants.

LC3/LGG-1 aggregates are suppressed in a *C. elegans pink-1* mutant

We used genetic crosses with a *C. elegans* Pink1 mutant to determine more directly whether Fis1 affects mitophagy. The *C. elegans pink-1(tm1779)* allele has a deletion encompassing the translation initiation site and the amino-terminal mitochondrial targeting sequence of Pink1. It therefore seems likely that this is a null allele with little or no mitophagy. One measure of mitophagy in mammalian cells is the formation of individual mitophagosomes, which appear as small spots with colocalizing LC3 and mitochondrial markers. Formation of these spots is blocked by dominant-negative mutations in Drp1 (Frank *et al.*, 2012). We looked for similar spots of colocalization in *C. elegans* using our LGG-1 and mitochondrial markers. We observed colocalizing spots of ~1-µm diameter in untreated wild-type and Fis1 mutant animals (Figure 4, A and B) and significantly reduced number of spots in Mff double and Fis1 Mff quadruple mutant strains (Figure 4, A and B). Spots that are still formed in Mff mutants could result from the low levels of fission that occurs in these animals, or they may represent stalled mitophagosome intermediates. In contrast, *pink-1* single and *pink-1 fis-1 fis-2* triple mutant animals had no colocalizing spots, as expected for a complete block of mitophagy (Figure 4, A and B). These results suggest that initial steps in the formation of mitophagosomes are not inhibited by Fis1 mutations, but their number is reduced by Mff mutations and eliminated by the Pink1 mutation.

The *pink-1 fis-1 fis-2* triple mutant also had fewer and smaller LGG-1 aggregates than the Fis1 double mutant (Figure 4C). The

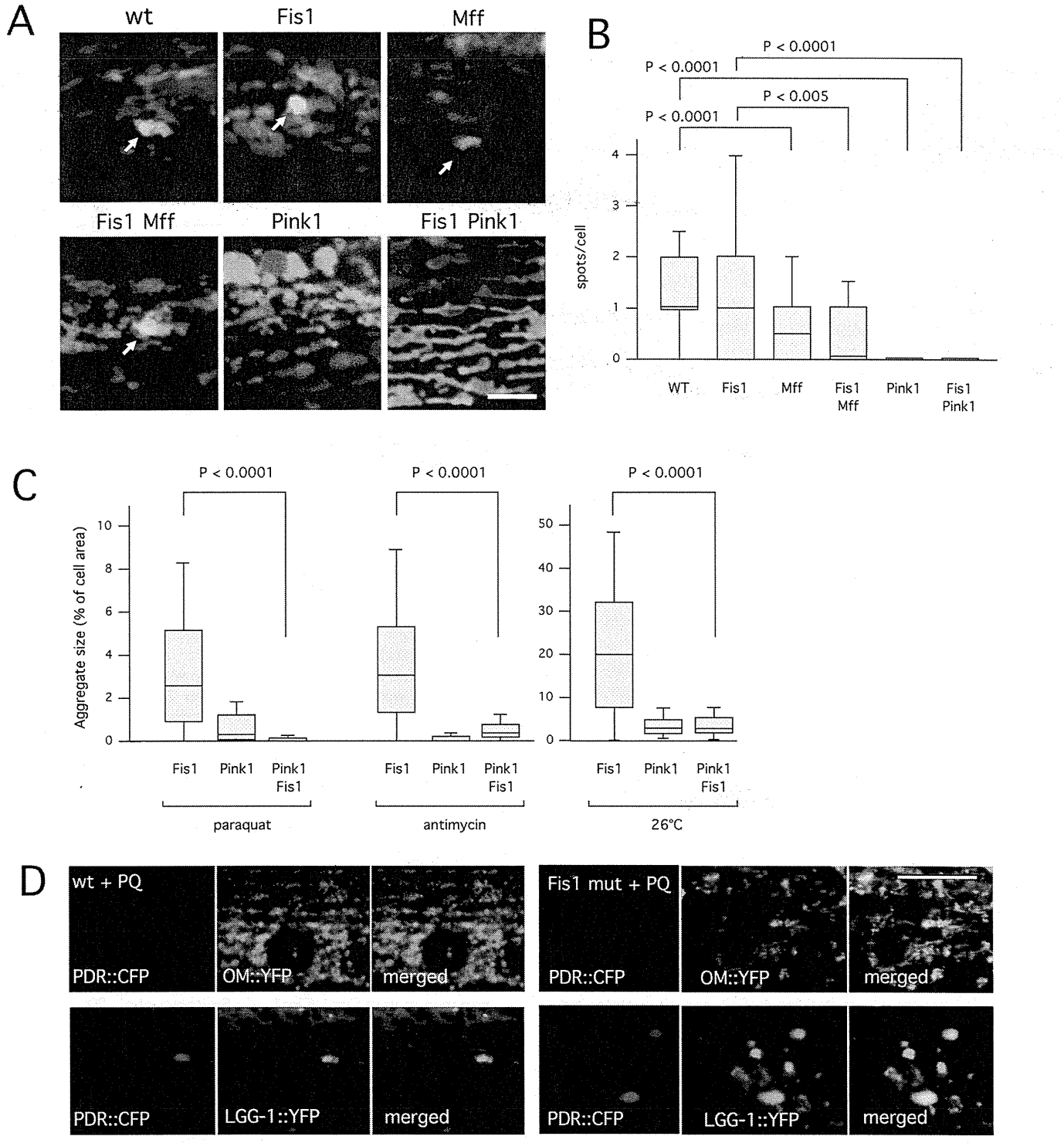

FIGURE 4: A mutation in Pink1 reduces the number of nascent mitophagosomes and suppresses aggregate formation in Fis1 mutants. (A) Mitophagy was induced by treatment for 1 h with Paraquat. Nascent mitophagosomes were detected by colocalization of CFP::LGG-1 (red) and YFP::TOM70 (green) in spots on the surface of mitochondria (arrows). As long as these spots were small (≤1 µm in diameter) they were classified as mitophagosomes. Larger spots were classified as aggregates. Strains were *fis-1(tm1861); fis-2(gk414)*, *pink-1(tm1799)*, and *pink-1(tm1799) fis-1(tm1861); fis-2(gk414)* (labeled as Fis1, Pink1, and Fis1 Pink1, respectively). Bar, 5 µm. (B) Boxplots showing the occurrence of CFP and YFP colocalizing spots per cell in the different strains (≥100 cells per condition, unpaired Student's *t* test). (C) Paraquat-, antimycin A–, and temperature-induced aggregate formation in Fis1, Pink1, and Fis1 Pink1 mutant strains. Aggregate sizes are shown as percentages of cell surface area. Box plots represent ≥40 cells per condition (*p* values determined with unpaired Student's *t* test). (D) *C. elegans* muscle cells labeled with (top) Parkin (PDR::CFP, red) and YFP::TOM70 (green) or (bottom) Parkin (PDR::CFP, red) and YFP::LGG-1 (green). Left, wild type, and right, Fis1 mutants treated with Paraquat (PQ). Bar, 10 µm.

suppression of LGG-1 aggregates by mutations in Pink1 could be due to changes in mitochondrial fission or fusion rates, since Pink1 and Parkin trigger the degradation of mitofusins in mammalian cells (Tanaka *et al.*, 2010), and they may activate mitochondrial fission in *Drosophila* (Yang *et al.*, 2008). Mitochondrial connectivity was somewhat increased in worms grown with Pink1 RNAi and in *pink-1(tm1779)* animals, but the effect was modest, and there were also other morphological abnormalities suggestive of mitochondrial defects (Supplemental Figure S4, A and B). Although this last experiment does not help decide between a role for Pink1 in fission or fusion, the foregoing experiments with aggregates and colocalizing spots do indicate that LGG-1 aggregates in Fis1 mutants are an aberrant product of Pink1-induced mitophagy. CFP-tagged Parkin also accumulates in LGG-1 aggregates in the Fis1 mutants, further suggesting that they are products of aberrant mitophagy (Figure 4D).

Mammalian Fis1$^{-/-}$ cells also form LC3 aggregates through stress-induced fission

Because of the importance of mitophagy for neurodegenerative diseases such as Parkinson's (Youle and Narendra, 2011) and the lack of an obvious fission defect in Fis1$^{-/-}$ HCT116 cells (Otera *et al.*, 2010), we asked whether mammalian Fis1 could instead contribute to mitophagy as it does in worms. To complement the studies with the Fis1$^{-/-}$ cells, we generated an HCT116 cell line in which both alleles of the Mff gene were deleted (Figure 5A). Mff$^{-/-}$ cells have more elongated mitochondria than either wild-type or Fis1$^{-/-}$ cells, consistent with the role of Mff in recruiting Drp1 to mitochondria (Figure 5, B and C). It is worth noting that the phenotype of Mff$^{-/-}$ cells was not as strong as that of Mff siRNA–treated cells (Gandre-Babbe and van der Bliek, 2008), suggesting that there may be some adaptation through alternative recruitment proteins similar to *C. elegans* Mff mutants.

As previously reported, mutations in Fis1 do not normally affect the balance between mitochondrial fission and fusion (Figure 5, B and C), but it has also been suggested that Fis1 specifically affects stress-induced fission (Kim *et al.*, 2011). To test this, we acutely induced fission by treating HCT116 cells for 10 min with antimycin A or carbonyl cyanide *m*-chlorophenyl hydrazone (CCCP) and monitored the effects on mitochondrial morphology by fluorescence microscopy. Almost all wild-type cells treated with antimycin A had fragmented mitochondria under these conditions, but fewer Fis1$^{-/-}$ cells had fully fragmented mitochondria (Figure 5C). Fragmentation was complete after prolonged incubations, so Fis1 is not required for fission, but mutations in Fis1 can slow stress-induced fission. This slowing was not observed with CCCP (Figure 5C), suggesting that CCCP and antimycin A trigger mitochondrial fission in different ways. Similar differences were previously observed with CCCP- and etoposide-treated Fis1$^{-/-}$ cells (Loson *et al.*, 2013). We conclude that mutations in Fis1 have modest effects on fission induced by certain chemicals, such as antimycin A, but not by CCCP.

To test whether mammalian Fis1 mutants form LC3 aggregates, we treated the Fis1$^{-/-}$ cells with antimycin A. Because HCT116 cells have undetectably low Parkin expression levels (Ding *et al.*, 2010), these cells were transfected with mCherry-Parkin, along with green fluorescent protein (GFP)–LC3 to follow aggregate formation. The diffuse and cytosolic pattern of GFP-LC3 in wild-type cells is converted to large aggregates in Fis1$^{-/-}$ cells that are treated with antimycin A. In contrast, parental HCT116 cells and Mff$^{-/-}$ cells have few or much smaller aggregates (Figure 6, A and C). Mitochondrial markers colocalize with GFP-LC3 aggregates in Fis1$^{-/-}$ cells like they

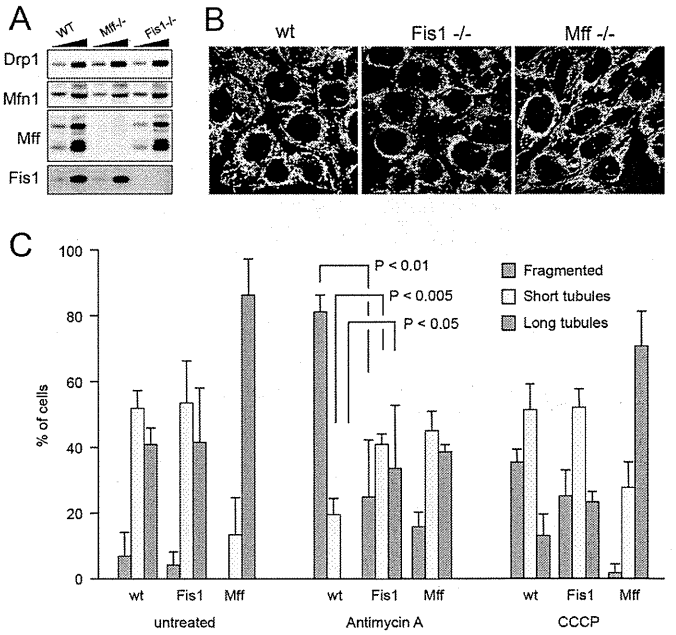

FIGURE 5: Characterization of mammalian Fis1$^{-/-}$ and Mff$^{-/-}$ cells. (A) Western blots showing that Fis1 is absent from HCT116 Fis1$^{-/-}$ cells and Mff is absent from HCT116 Mff$^{-/-}$ cells. Drp1 and Mfn1 expression levels were not changed. Low and high amounts of cell lysates were loaded on the gel for comparison. (B) Mitochondrial morphologies detected with anti-Tom20 antibody immunostaining in wild-type, Mff$^{-/-}$, and Fis1$^{-/-}$ cells. (C) Quantification of mitochondrial morphologies in HCT116 wild-type, Fis1$^{-/-}$, and Mff$^{-/-}$ cells that were left untreated or were treated for 10 min with antimycin A or CCCP. These cells were stained with MitoTracker Green and photographed. Thirty images for each condition were coded and pooled with the images for other conditions, allowing blind classification. Cells were classified as having predominantly fragmented, short tubular, or long tubular mitochondria. Mean and SD for three independent experiments. *p* values were determined with an unpaired Student's *t* test.

do in *C. elegans* Fis1 mutants. The potassium ionophore valinomycin can similarly induce GFP-LC3 aggregates in HCT116 Fis1$^{-/-}$ cells (Supplemental Figure S5A). Immuno–electron microscopy shows that these aggregates contain clusters of mitochondria surrounded by LC3-decorated membranes (Figure 6D). In addition, dominant-negative mutant Drp1 (Drp1$_{K38A}$; Smirnova *et al.*, 2001) suppresses LC3 aggregate formation in mammalian Fis1$^{-/-}$ cells (Figure 6, B and C). We conclude that mammalian Fis1 mutants form LC3 aggregates and that these aggregates depend on Drp1.

Longer incubations with antimycin A caused there to be more LC3 aggregates (Supplemental Figure S5B). Transfections with Fis1 shRNA followed by treatment with antimycin A also gave rise to a high percentage of cells with LC3 aggregates (Supplemental Figure S5, C–E), whereas these percentages were reduced with Fis1$^{flox/-}$ cells and with Fis1$^{-/-}$ cells that were transiently transfected with Fis1 (Supplemental Figure S5, C, F, and G). These results confirm that the effects are specific for Fis1. To determine whether the LC3 aggregates are caused by aberrant mitophagy, we manipulated Parkin expression in Fis1$^{-/-}$ cells. Similar to the effects of *C. elegans* Pink1 mutations, we find that Parkin expression is required for LC3 aggregate formation in mammalian cells (Supplemental Figure S5H). These results suggest that LC3 aggregates are caused by aberrant mitophagy.

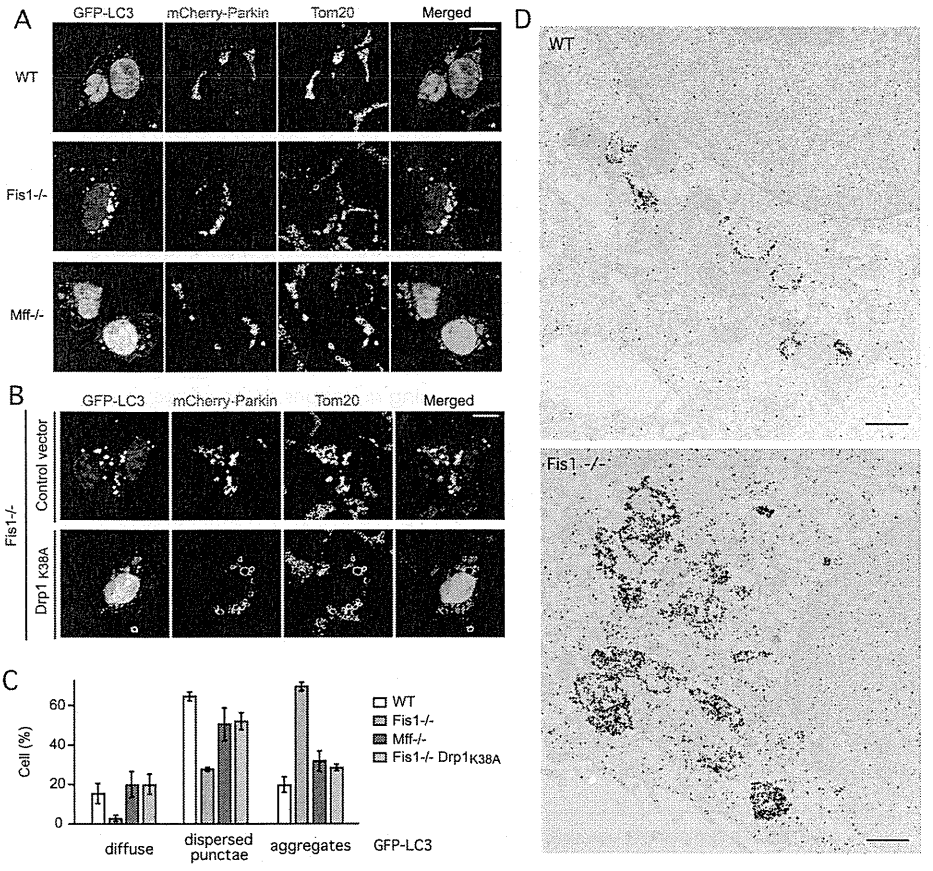

FIGURE 6: Large LC3 aggregates are formed in Fis1$^{-/-}$ mammalian cells. (A) LC3 aggregates induced by antimycin A in HCT116 Fis1$^{-/-}$ cells but not wild-type (WT) or Mff$^{-/-}$ cells. HCT116 WT, Fis1$^{-/-}$, and Mff$^{-/-}$ cells were transfected with GFP-LC3 and mCherry-Parkin expression constructs, followed 18 h later by 3-h incubation with antimycin A to induce Parkin translocation onto mitochondria and immunostaining with anti-Tom20 antibody to label mitochondria. Bar, 10 μm. (B) GFP-LC3 aggregate formation is largely suppressed by transfection with a dominant-negative Drp1 mutant (Drp1$_{K38A}$). Transfections and drugs as in A. (C) Quantification of results in A and B by classifying LC3 distributions as diffuse cytosolic, dispersed punctae, or large aggregates. Untreated cells (no antimycin A) had no aggregates (unpublished data). Mean and SD for three independent experiments (>100 cells/experiment). (D) Immunogold-labeled GFP-LC3 in an HCT116 WT cell and a Fis1$^{-/-}$ cell. Bar, 1 μm.

A classic method for studying effects on mitophagy is assessment of mitochondrial clearance in HeLa cells that overexpress GFP-Parkin (Narendra *et al.*, 2008). These cells were transfected with scrambled or Fis1 siRNA oligonucleotides, treated for 24 h with antimycin A, and monitored for clearance with fluorescence microscopy and Western blots. However, the results show no obvious differences in clearance between Fis1 siRNA and control cells (Figure 7, A and B). Moreover, clearance was suppressed to the same extent in both cell types when cells were additionally treated with the lysosome fusion inhibitor bafilomycin A1 (Yamamoto *et al.*, 1998; Figure 7B). We conclude that mitophagic flux is unchanged, even though the dependence of LC3 aggregates on Pink1 and Parkin suggests that progression through the mitophagic pathway is abnormal.

To determine how mitophagy might be affected, we probed Western blots for p62 and LC3. We found that the levels of lipidated LC3 are increased in Fis1$^{-/-}$ cells when compared with wild-type cells, especially after treatment with antimycin A (Figure 7C). Effects on LC3 lipidation were similarly observed with valinomycin (Figure 7D), which also induces mitophagy (Rakovic *et al.*, 2010). However, the turnover of p62 was not increased in Fis1$^{-/-}$ cells treated with antimycin A or valinomycin, despite increased LC3 lipidation (Figure 7, C and D). In fact p62 degradation was reduced, suggesting that mutations in Fis1 slow the access of nascent mitophagosomes to downstream degradation processes. To further investigate which stages of autophagy are affected by Fis1, we also incubated valinomycin-treated cells with the downstream inhibitor bafilomycin A1 (Yamamoto *et al.*, 1998). This treatment did not further increase the amount of LC3 lipidation or decrease the amount of p62 turnover, showing that inhibition by mutations in Fis1 occurs upstream of the actions of bafilomycin A1. Remarkably, Mfn1 is degraded to the same extent in wild-type and Fis1$^{-/-}$ cells treated with antimycin A (Figure 7D), showing that deletion of Fis1 does not inhibit the previously described Pink1- and Parkin-dependent proteosomal degradation of Mfn1 or entry onto the mitophagy pathway (Tanaka *et al.*, 2010). Together these data suggest that the rates of entry into and exit from the mitophagy pathway are unchanged. Instead, an intermediate stage may be slowed down.

To test whether the increased lipidation of LC3 is caused by macroautophagy, we grew wild-type and Fis1$^{-/-}$ cells under two conditions that induce macroautophagy (starvation and calcium phosphate precipitation; Gao *et al.*, 2008). Neither treatment caused changes in LC3 lipidation in Fis1$^{-/-}$ cells when compared with wild-type cells, nor are aggregates formed in starved Fis1$^{-/-}$ cells, suggesting that Fis1 plays no role in starvation-induced macroautophagy (Figure 7, E and F). We conclude that human Fis1 acts during the mitophagy process before defective mitochondria are fully eliminated by core autophagy proteins.

Drp1 enters into a complex with Fis1 and ER proteins at the interface between mitochondria and ER

To further investigate processes affected by Fis1, we conducted coimmunoprecipitation experiments with Drp1. It was previously shown that overexpressed Mff and to a lesser extent overexpressed Fis1 will coimmunoprecipitate with Drp1 when a membrane-permeable cross-linker is added before cell lysis (Otera *et al.*, 2010). We were unable to coimmunoprecipitate endogenous Fis1 under these conditions but were able to coimmunoprecipitate endogenous Mff (Figure 8A). This situation changed dramatically upon treatment with CCCP. After 20 min, endogenous Fis1 was readily detectable in coimmunoprecipitates, while at the same time the signal for Mff appeared to decrease. This decrease may reflect transfer of Drp1 from Mff to Fis1 or decrease in the total amount of Drp1 on mitochondria because of completing the fission cycle.

It was previously shown that Drp1 can bind to Fis1 when it is phosphorylated at Ser-600 by Ca/Cam kinase Iα (Han *et al.*, 2008). Independently, it was shown that this residue is also phosphorylated by Cdk1, Rock1, and protein kinase C δ when fission is induced (Taguchi *et al.*, 2007; Qi *et al.*, 2011; Wang *et al.*, 2012). We tested whether Drp1 mutations that mimic the dephosphorylated or

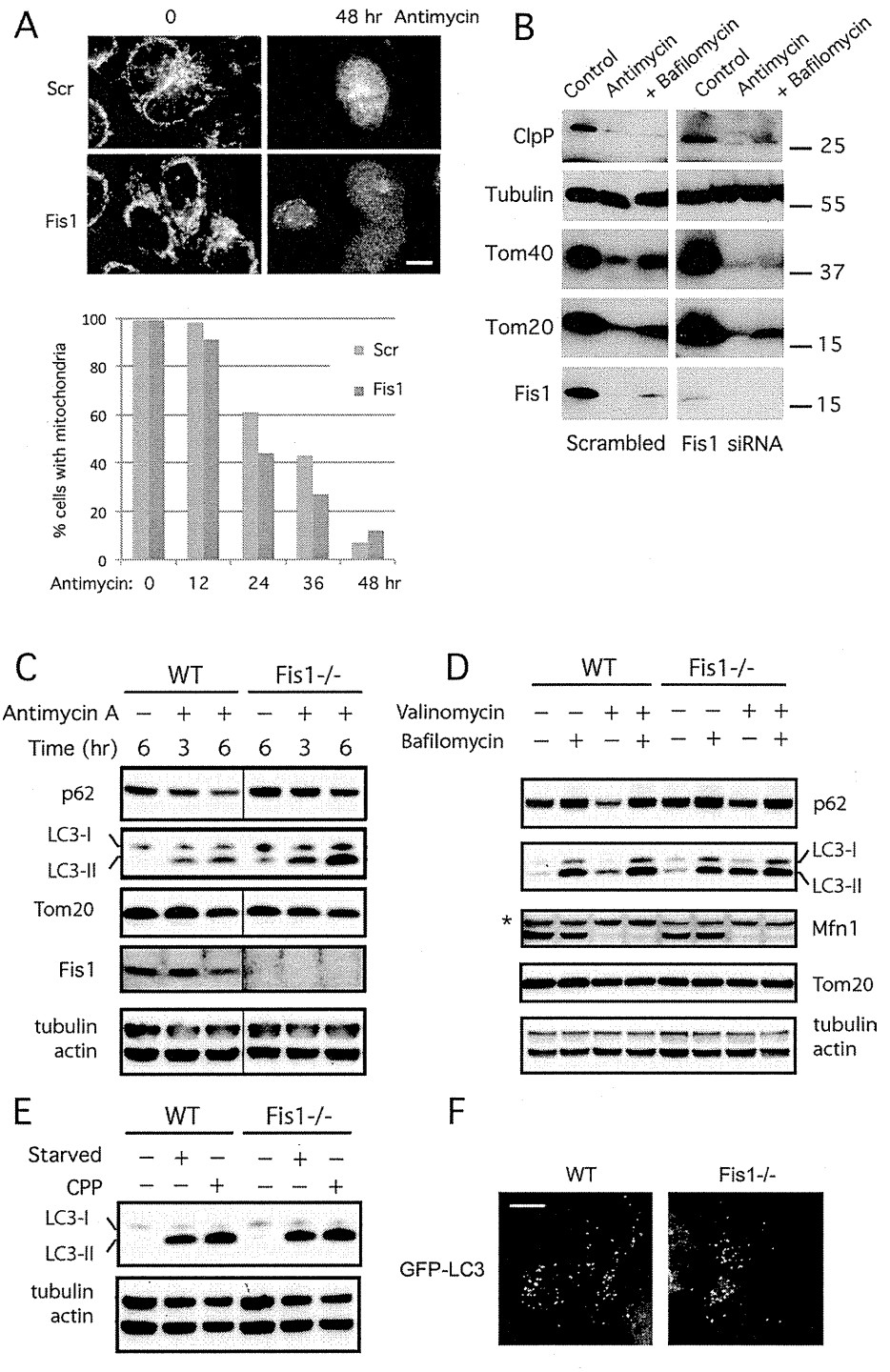

FIGURE 7: Fis1 acts before fusion to lysosomes in mammalian cells. (A) Clearance of mitochondria detected with fluorescence. HeLa cells that stably express GFP-Parkin were transfected with scrambled or Fis1 siRNA oligonucleotides and then treated for the indicated amounts of time with antimycin A. Cells were fixed and stained with Tom20 antibody (shown for 0- and 48-h treatments in the fluorescence images; bar, 10 μm). One hundred or more cells were assessed for the presence mitochondria and dispersal of Parkin as independent criteria at the time points shown in the histogram. (B) Clearance of mitochondria detected with Western blots. GFP-Parkin–expressing HeLa cells were transfected with siRNA and incubated for 48 h with solvent (dimethylsulfoxide), antimycin A, or antimycin A plus bafilomycin A1. Western blots were probed with antibodies for a mitochondrial matrix protein (ClpP), a cytosolic protein (tubulin), and three mitochondrial outer membrane proteins (Tom20, Tom40, and Fis1). The results show that mitochondrial outer membrane and matrix proteins are degraded to similar degrees in scrambled and Fis1 siRNA cells. (C) Western blots show accumulation of lipidated LC3 and inhibition of p62 degradation in Fis1$^{-/-}$ cells treated with antimycin A. HCT116 WT and Fis1$^{-/-}$ cell lines with stable EYFP-Parkin expression were treated with antimycin A for 3 or 6 h before cell lysis and immunoblotting. (D) Valinomycin induces increased LC3 lipidation in Fis1$^{-/-}$ cells, similar to antimycin A treatment, but this increase does not reflect an overall increase in autophagy, as shown with a block in further degradation by bafilomycin A1, nor does it reflect a block in mitochondrial degradation, as shown by the continued degradation of Mfn1 in valinomycin-treated Fis1$^{-/-}$ cells. HCT116 WT and Fis1$^{-/-}$ cell lines with stable enhanced YFP-Parkin expression were incubated for 1 h with or without valinomycin, followed by 5 h with or without bafilomycin A1. The asterisk indicates a nonspecific band. (E) Macroautophagy does not cause more LC3 lipidation in Fis1$^{-/-}$ than in WT cells. Macroautophagy was induced in EYFP-Parkin expressing HCT116 WT and Fis1$^{-/-}$ cells by 6-h amino acid starvation or with 4-h incubation with calcium phosphate precipitate (CPP). (F) Lack of LC3 clustering in cells with starvation-induced macroautophagy. GFP-LC3–transfected HCT116 WT and Fis1$^{-/-}$ cells were subjected to 6-h amino acid starvation and analyzed by fluorescence microscopy. Bar, 10 μm.

phosphorylated states of Ser-600 promote coimmunoprecipitation with endogenous Fis1 and conversely whether transfected FLAG-tagged Fis1 coimmunoprecipitates either one or both of the Drp1 mutants. We observed robust coimmunoprecipitation with Drp1(S600D) but not Drp1(S600A), suggesting that phosphorylation at Ser-600 is enough to drive Drp1 into a complex with Fis1 (Figure 8B).

We tested whether the interactions promoted by the phosphorylation of Drp1 contribute to LC3/LGG-1 aggregate formation, using mutations in the corresponding phosphorylation site of worm Drp1. We expressed DRP-1(S590D) and DRP-1(S590A) in *drp-1(tm1108)* animals, which have no endogenous Drp1. Both mutant proteins restored mitochondrial fission, as shown by tubular and fragmented mitochondria, in contrast to the *drp-1(tm1108)* strain by itself, which has highly connected mitochondria (Figure 8C). Paraquat and antimycin A induced more and larger LGG-1 aggregates in worms with DRP-1(S590A) than in worms with DRP-1(S590D) or wild-type DRP-1 transgene (Figure 8D). DRP-1(S590A) thereby mimics the effects of Fis1 deletions in vivo. We conclude that Drp1 phosphorylation defects cause LC3/LGG-1 aggregate formation similar to Fis1 defects, suggesting that critical interactions with phosphorylated Drp1 prevent aggregate formation.

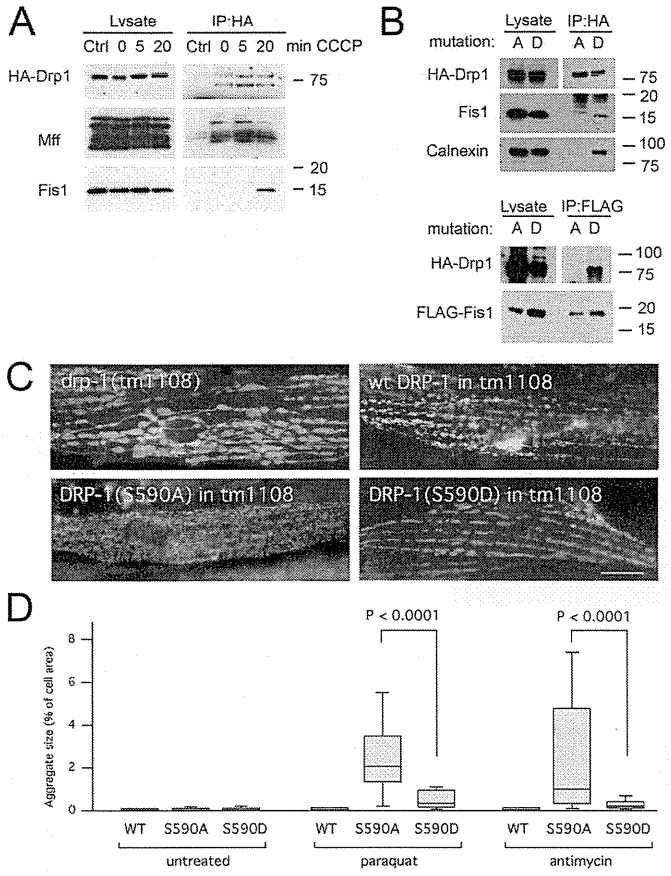

FIGURE 8: Drp1 enters into a complex with Fis1 when fission is induced. (A) HeLa cells were transfected with HA-Drp1 and treated for the indicated amounts of time with CCCP to induce mitochondrial fission. The cells were then treated with DSP and lysed with 1% SDS before coimmunoprecipitation with mock (Ctrl) or mouse HA antibody. Western blots were probed with rabbit anti-HA, Mff, and Fis1 antibodies. (B) Top, results of HeLa cell transfections with HA-Drp1(S600A) or HA-Drp1(S600D), treatment with DSP, coimmunoprecipitation with HA antibody, and probing for endogenous Fis1. Calnexin also coimmunoprecipitates with HA-Drp1(S600D) but not with HA-Drp1(S600A). Bottom, results obtained after cotransfection with FLAG-tagged Fis1 and coimmunoprecipitation with FLAG antibody. (C) Mitochondrial morphologies in *C. elegans* muscle cells detected with the mitochondrial outer membrane marker ($P_{myo\text{-}3}$*::Tom70::YFP*). Mitochondria in *drp-1(tm1108)* worms are highly connected. Mitochondrial fission was restored with transgenic DRP-1(wt), transgenic DRP-1(S590A), or transgenic DRP-1(S590D). Bar, 10 μm. (D) LGG-1 aggregate sizes in muscle cells of *drp-1(tm1108)* worms treated with chemicals as indicated. Mitochondrial fission was restored with transgenic DRP-1(wt), transgenic DRP-1(S590A), or transgenic DRP-1(S590D). Aggregate sizes are shown as percentages of cell surface area as in Figure 2B ($n > 40$ cells/condition, unpaired Student's *t* test).

To test which fission-inducing conditions promote Fis1 coimmunoprecipitation, we treated cells with antimycin A (mitophagic fission), the phorbol-ester phorbol-12-myristate-13-acetate (PMA; fission through kinase activation), and staurosporine (apoptotic fission). We found that each of these chemicals strongly increased coimmunoprecipitation of Fis1 with Drp1 (Figure 9A). The effect was specific, because other mitochondrial outer membrane proteins (Tom20, Tom40, and VDAC) did not coimmunoprecipitate (Figure 9A). We conclude that Drp1 does not normally bind to Fis1 but can coimmunoprecipitate Fis1 when fission is induced under a range of conditions, including apoptosis and mitophagy.

We also tested whether Drp1 becomes part of a larger complex at the ER–mitochondrial interface (mitochondrion-associated membrane [MAM]), because Fis1 was previously shown to coimmunoprecipitate with Bap31 (an ER protein in the MAM; Iwasawa *et al.*, 2011). Our results show that hemagglutinin (HA)-tagged Drp1 coimmunoprecipitates endogenous Bap31 and calnexin (another MAM protein; Myhill *et al.*, 2008) when cells are treated with antimycin A or PMA (Figure 9A). These treatments induce mitochondrial fragmentation (Supplemental Figure S5I), but the downstream effects are different. Antimycin A induces mitophagy, whereas PMA induces mitochondrial fission, and over a longer period it leads to apoptosis. A third treatment, in which we used staurosporine to more quickly induce apoptosis, does promote coimmunoprecipitation of Fis1 with Drp1, but there was less coprecipitation of calnexin and little or none of Bap31, most likely because Bap31 is cleaved by a caspase during apoptosis (Iwasawa *et al.*, 2011). We conclude that different fission-inducing chemicals cause Drp1 to enter into a fission complex with Fis1 and other MAM proteins.

Similarly, calnexin was found to coimmunoprecipitate with HA-Drp1(S600D) but not HA-Drp1(S600A) (Figure 8B). These results suggest that the S600D mutation promotes entry of Drp1 into the fission complex in the MAM. To determine whether Fis1 is required for this step, we cotransfected Fis1 siRNA oligonucleotides. We noted that Fis1 siRNA caused a reduction in the overall amounts of calnexin but did not prevent coimmunoprecipitation of Bap31 and calnexin with Drp1, suggesting that Fis1 is not required for complex formation (Figure 9B). Instead, Fis1 may contribute to other aspects of fission—for example, helping to coordinate changes at the ER–mitochondrial interface with downstream effects.

ER has been connected with mitochondrial fission (Friedman *et al.*, 2011) and is a source of autophagosomal membrane (Hamasaki *et al.*, 2013), raising the possibility that ER contributes to the aggregates in Fis1 mutants. In support, we can detect an ER marker in the LGG-1 aggregates in *C. elegans* Fis1 mutants (Figure 9C). Relevance of the MAM for aggregate formation was tested by treating worms with RNAi for *C. elegans* PACS-2 (an adaptor for calnexin) and Bap31 homologues (Figure 9D). We found that PACS-2 RNAi reduces the size and prevalence of LGG-1 aggregates in Paraquat-treated Fis1-mutant animals (Figure 9D). Because PACS-2 is required for maintaining the ER–mitochondrial interface (Myhill *et al.*, 2008), our result suggests that the MAM contributes to the formation of LGG-1 aggregates in the Fis1 mutant. Taken together, our data show that Drp1 enters into a complex at the MAM when mitochondrial fission is induced. This complex promotes the orderly and efficient removal of defective mitochondria. Fis1 is part of the MAM complex and contributes to a late stage of the removal process but is not required for entry of Drp1 into the MAM or fission.

DISCUSSION

Although Fis1 plays a well-established role in yeast mitochondrial fission (Mozdy *et al.*, 2000), the functions of Fis1 in metazoans have remained a matter of debate. Earlier experiments suggested that Fis1 contributes to mitochondrial fission in mammalian cells (James *et al.*, 2003), and it was suggested that Fis1 can promote stress-induced fission (Kim *et al.*, 2011), but these functions were challenged by the apparent absence fission defects in Fis1$^{-/-}$ cells (Otera *et al.*, 2010). Modest effects on fission and partial redundancy with Mff have, however, also been observed (Loson *et al.*, 2013). Our data confirm this modest effect with specific fission-inducing conditions,

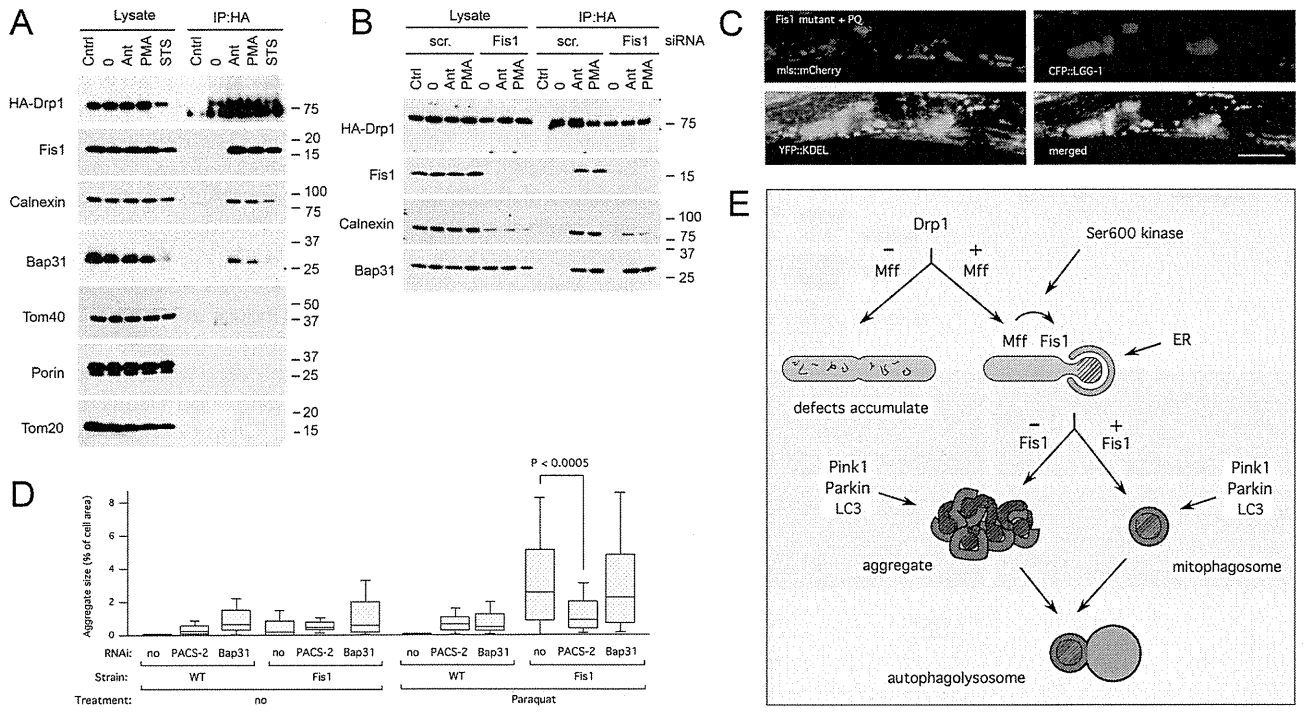

FIGURE 9: The Drp1-Fis1 complex also contains ER proteins. (A) HeLa cells were transfected with HA-Drp1 and treated as in Figure 8A, but instead of CCCP they were incubated for 3 h with antimycin A (Ant), phorbol myristic acid (PMA), or staurosporine (STS), followed by cross-linking and lysis with RIPA. Blots were probed with HA, Fis1, calnexin, Bap31, Tom40, porin, and Tom20 antibodies. Bap31 is partially degraded by caspase 8–dependent cleavage when cells are treated with staurosporine (Iwasawa *et al.*, 2011), but this treatment clearly also induces coimmunoprecipitation with Drp1. (B) HeLa cells were transfected with scrambled or Fis1 siRNA oligonucleotides, followed after 2 d by transfection with HA-Drp1, and then treated as in A. Surprisingly, the overall amount of calnexin was reduced by Fis1 siRNA, but this did not prevent coimmunoprecipitation with HA-Drp1. (C) Triple labeling with mls::mCherry (red), the ER marker ss:YFP::KDEL (green), and CFP::LGG-1 (blue). The images show that LGG-1 clusters contain ER. Bar, 10 μm. (D) Aggregate sizes in muscle cells of wild-type worms and Fis1 mutants grown with RNAi for *C. elegans* PACS-2 (T18H9.7) or Bap31 (Y54G2A.18) homologues, followed by treatment with Paraquat. Aggregate sizes are shown as percentages of cell surface area. Boxplots represent ≥40 cells/condition (*p* values determined with unpaired Student's *t* test). (E) Diagram showing where Drp1, Mff, and Fis1 act during mitochondrial fission and subsequent degradation through mitophagy.

but they also reveal much more pronounced effects on downstream stages of removal through mitophagy. Mutations in Fis1 disrupt mitophagy by generating LC3/LGG-1 aggregates upon treatment with ROS-producing toxins such as Paraquat, antimycin A, and valinomycin. These aggregates are suppressed by mutations in Drp1 and Mff, showing that Fis1 acts in sequence with Mff during or after the mitochondrial fission process. We conclude that Fis1 can affect fission and is part of the larger fission complex but is not required for fission and has much more dramatic effects on an intermediate stage of the mitophagy pathway.

A range of different approaches for inactivating Fis1 in mammalian cells and worms give rise to LGG-1/LC3 aggregates, showing that these aggregates do not result from secondary mutations in other genes. Specificity is further supported by our ability to suppress aggregates through Fis1 overexpression in *C. elegans*. Our data also show that the aggregates were not a secondary response to starvation- or heat shock–induced macroautophagy. Several earlier reports suggested that Fis1 might affect autophagy. It was shown, for example, that Fis1 siRNA reduces the number of mitophagy intermediates (Twig *et al.*, 2008), whereas Fis1 overexpression can induce autophagy in mammalian cells (Gomes and Scorrano, 2008). It was also suggested that *C. elegans* Fis1 might indirectly affect fission and autophagy (Breckenridge *et al.*, 2008; Kim *et al.*, 2011), and *Drosophila* studies showed genetic interactions with Pink1 and Parkin mutants (Yang *et al.*, 2008). Our results confirm and extend these observations by showing that LGG-1/LC3 aggregates form when Fis1 mutants are treated with chemicals that disrupt mitochondrial function. These aggregates can contain mitochondrial and ER markers, along with tagged versions of Pink1 and Parkin proteins. More important, they are suppressed by mutations in Pink1 and Parkin genes. Together these results show that the LGG-1/LC3 aggregates in Fis1 mutants are products of aberrant mitophagy.

Mitochondrial clearance, resulting from prolonged incubation with chemicals such as CCCP, is inhibited by mutations in Pink1 and Parkin (Narendra *et al.*, 2008). We find, however, that mutations in Fis1 have little or no effect on clearance. Mfn1 is still degraded at early time points, and the remaining mitochondrial proteins are removed at later time points after incubating in Fis1 mutants with mitochondrial toxins. If clearance is not blocked, then why is there a buildup of LGG-1/LC3 aggregates in Fis1 mutants? Our Western blots show that mutations in Fis1 increase the amount of LC3 but not of p62. There is no further increase when bafilomycin A is added, showing that mutations in Fis1 do not increase the total amount of mitophagy or affect later stages of mitophagy. It seems likely that the total number of mitochondria that enter the mitophagy pathway remains the same but mutations in Fis1 slow the disposal process at a

stage before fusion to lysosomes, causing a temporary buildup of intermediates in the disposal pathway and resulting in LC3/LGG-1 aggregates. On the basis of these results, we propose that Fis1 contributes to mitophagy, after Mff and Drp1 initiate mitochondrial fission but before defective mitochondrial fragments are fully engaged in the degradation process (Figure 9E).

Does Fis1 couple fission with mitophagy? Our data show that Drp1 can coimmunoprecipitate Fis1 when mitochondrial fission is chemically induced. Drp1 then also coimmunoprecipitates ER proteins, such as calnexin and Bap31, suggesting that Fis1 is part of a larger protein complex at the ER–mitochondrial interface. The inclusion of ER proteins in the fission complex is consistent with previously observed mitochondrial fission events at the MAM (Friedman *et al.*, 2011) and with active recruitment of Drp1 to the MAM by an ER protein (Korobova *et al.*, 2013). Proteins in the MAM also promote apoptosis (Alirol *et al.*, 2006), as shown by the contributions of Bap31 and Fis1 to this process (Iwasawa *et al.*, 2011). It therefore seems likely that Fis1 acts at a critical junction in the fission process when the products of fission are directed toward normal mitochondrial homeostasis, mitophagy, or apoptosis.

Little is known about the organization of the fission complex or how it might affect the different outcomes of the fission process. Drp1 can bind to Fis1 in vitro (Yoon *et al.*, 2003; Han *et al.*, 2008), but our data do not show a requirement for direct interactions in vivo. Drp1 can still coimmunoprecipitate Bap31 and calnexin when Fis1 is knocked down, and fission is at best mildly impaired in Fis1 mutants. Moreover, binding between Fis1 and a Rab-GAP (Onoue *et al.*, 2013) and between Fis1 and Bap31 (Iwasawa *et al.*, 2011) raises the possibility that Fis1 has other functions during or after fission. Further studies of these interactions may help clarify the roles of Fis1 in mitophagy and apoptosis. Our results do, however, already show that Fis1 acts at a critical junction in major stress-response pathways. Depending on the stress conditions, Fis1 can contribute to apoptosis or to the orderly disposal of defective mitochondria through mitophagy.

MATERIALS AND METHODS

Materials

Paraquat (MP Biomedicals, Santa Ana, CA), A23187, and ionomycin (Calbiochem/Merck, Darmstadt, Germany) were used at the indicated concentrations. Phorbol myristic acid (Calbiochem) was used at 1 μM. CCCP, antimycin A, valinomycin, and bafilomycin A1 were from Sigma-Aldrich (St. Louis, MO) and used at final concentrations of 20 μM, 40 μg/ml, 10 μM, and 100 nM, respectively. Staurosporine (Tocris Biosciences, Bristol, UK) was used at 2 μM. Mff and Mfn1 antibodies were described previously (Gandre-Babbe and van der Bliek, 2008; Tanaka *et al.*, 2010). The following antibodies were purchased: FLAG (Genescript, Piscataway, NJ), HA (Roche, Basel, Switzerland), Tom20, Tom40, Parkin, and normal mouse immunoglobulin G (IgG; Santa Cruz Biotechnology, Santa Cruz, CA), calnexin and Drp1 (BD Transduction Laboratories, Franklin Lakes, NJ), p62 (Abnova, Taipei City, Taiwan), porin (MitoSciences, Eugene, OR), LC3B (Sigma-Aldrich), Fis1 (Alexis Biochemicals and Proteintech, Farmingdale, NY), α-tubulin (Invitrogen, Carlsbad, CA), and actin (Sigma-Aldrich). Rabbit polyclonal antibodies were generated against polypeptide fragments of *C. elegans* DRP-1 protein and used along with other antibodies to probe blots of *C. elegans* extracts as described previously (Head *et al.*, 2011).

C. elegans strains, plasmids, and imaging

C. elegans fis-1(tm1867), *mff-1(tm2955)*, *mff-2(tm3041)*, *drp-1(tm1108)*, and *pink-1(tm1779)* strains were provided by S. Mitani (National Bioresource Project of Japan, Tokyo Women's Medical University School of Medicine, Tokyo, Japan). The *fis-2(gk414)* strain was provided by the *Caenorhabditis* Genetics Center (University of Minnesota, St. Paul, MN). These strains were backcrossed four to six times with wild-type N2 animals to remove adventitious mutations. Transgenic strains were made by microinjection, using *rol-6* as a transformation marker. Feeding RNAi was as described (Timmons *et al.*, 2001). Full-length *fis-1*, *fis-2*, *mff-1*, *and mff-2* cDNAs were cloned in the pPD96.52 expression vector with the *myo-3* promoter for muscle cell expression as described previously (Head *et al.*, 2011). YFP coding sequences (Labrousse *et al.*, 1999) were added into the *Nhe*I site of the pPD96.52 expression before FIS-1 coding sequences to create the $P_{myo\text{-}3}$*::YFP::FIS-1* construct. Mitochondrial outer membrane and matrix markers with GFP derivatives under control of the *myo-3* promoter were described previously (Labrousse *et al.*, 1999). An mCherry marker was made by replacing GFP with mCherry coding sequences. The CFP::LGG-1 marker, modeled after a previously reported GFP::LGG-1 construct (Melendez *et al.*, 2003), was made by cloning CFP and LGG-1 coding sequences behind the *myo-3* promoter in the pPD96.52 vector. The ER marker $P_{myo\text{-}3}$*::SS::YFP::KDEL* was described previously (Labrousse *et al.*, 1999). DRP-1(S590A) and DRP-1(S590D) mutants were made using QuikChange site-directed mutagenesis and $P_{myo\text{-}3}$*::DRP-1* (Labrousse *et al.*, 1999) as template. The *C. elegans* Parkin marker $P_{myo\text{-}3}$*::PDR-1::CFP* was made by PCR cloning in the pPD96.52 vector. Feeding RNAi for the peripheral benzodiazepine receptor was achieved with a bacterial construct for the corresponding gene (C41G7.3). Overexpression was achieved with the *myo-3* promoter fused to the coding region of C41G7.3. This construct was injected into an *rde-1(ne219)* (RNAi defective) to prevent antisense RNA.

To determine expression levels with qPCR, *C. elegans* cultures were synchronized with bleach, cultured with OP50 bacteria, and harvested as young adults. RNA was extracted by repeated freezing and thawing of worms suspended in TRIzol (Invitrogen). RNA preparations were treated with DNaseI, followed by cDNA synthesis using Thermoscript with protocols provided by the manufacturers (Invitrogen and Ambion/Life Technologies, Carlsbad, CA). Primers for qPCR were designed as in Haynes *et al.* (2007) with the primers TCGGTATGGGACAGAAGGAC and CATCCCAGTTGGTGACGATA for pan-actin (act-1,3,4), TCAATGGATTTCGGTTGGGA and ACGCTCCAACAGGATCTCTA for *bec-1* (T19E7.3), ACTTCCTCATCAGAAAACGC and TTCCTCGTGATGGTCCTGGT for *lgg-1* (C32D5.9), AGCCCAGGAAGCTCAAGAAG and GGAGACGATCGAATGTCTTT for p62 (T12G3.1), GGTTGAAGAGTCCGAGTTCT and AAGTTGGATGGATGTCTGTC for *let-363* (B0261.2), GGGAAGAAACGTGATCATCGA and CAGCCTCCTCATTAGCCTTG for *hsp-60* (Y22D7AL.5), and CAAACTCCTGTGTCAGTATCATGGAAGG and GCTGGCTTTGACAATCTTGTATGGAACG for *hsp-6* (C37H5.8.3). Each qPCR contained cDNA made from 1 μg of total RNA. qPCRs were performed in triplicate with SYBR Green reagent (Invitrogen) with annealing and extension at 63°C in an Mx3000P Thermal Cycler, followed by analysis with MxPro Software (Agilent, Santa Clara, CA). Dissociation curves confirmed individual PCR products. The *Ct* values were converted to percentages, and expression ratios were calculated for three independent RNA preparations.

Where indicated, worms were incubated for 1 h at 20°C in M9 media with 80 mM Paraquat and bacteria or for 2 h with 1 mM antimycin A, after which they were allowed to recover on nematode growth media plates with bacteria but no drugs for 5 and 4 h, respectively, at 20°C. Mitochondrial fragmentation was induced by

incubating worms for 1 h at 20°C in M9 medium with 50 µM A23187 or ionomycin. For temperature shift experiments, worms were grown for 48 h at 25 or 26°C before imaging. Brood sizes were determined by placing single L1 larvae on individual plates and counting progeny that survive to the L4 larval stage. For subcellular fractionation, synchronized cultures of *C. elegans* were harvested, homogenized with a glass tissue homogenizer, and fractionated by differential centrifugation (Head *et al.*, 2011). The P2 fraction (14,000 × *g* pellet) was washed twice with STEG (250 mM sucrose, 5 mM Tris-HCl, 1 mM EGTA, pH 7.4) and protease inhibitors.

Fluorescence images of live worms were made with a Zeiss Axiovert 200M microscope equipped with a 100×/1.45 numerical aperture (NA) α-Plan-Fluar objective (Carl Zeiss, Jena, Germany) and an ORCA ER-CCD camera (Hamamatsu, Shizuoka, Japan). Images in the figures were processed with Photoshop (Adobe, San Jose, CA). Because the muscle cells that we used for this analysis are flat, we could approximate aggregate sizes by measuring their surface areas. These areas were measured by tracing cell and aggregate outlines with ImageJ software (National Institutes of Health, Bethesda, MD; 40 or more cells for each condition). Aggregate sizes are shown as percentages of cell area in boxplots. The horizontal line inside the box is the median. The bottom of the box shows where the first quartile ends and the second begins, and the top shows where the third quartile ends and the fourth begins. The whiskers show minimum and maximum values of the data set, as long as these values do not differ from the median by >1½ times the interquartile range.

Surface renderings of mitochondria and LGG-1 aggregates were made with stacks of 20 fluorescence images collected over a distance of 1 µm with a spinning disk confocal microscope (Marianas System; Intelligent Imaging Innovations, Santa Monica, CA). The images were processed with the three-dimensional software package provided by the manufacturer (Slidebook 5.5). Surface rendering was set with an outline width of 1 pixel and a threshold of 50% for the red channel (LGG-1 fluorescence) and 25% for the green channel (mitochondrial outer membrane marker). Where indicated, opacity of the red channel was set at 50% to visualize embedded mitochondria. Otherwise, opacity was set at 100%.

Mammalian cell culture and transfections

Fis1$^{-/-}$, Fis1$^{flox/-}$, and HCT116 with lentivirus-infected control shRNA and Fis1 shRNA were reported previously (Otera *et al.*, 2010). Transfections were done at 18–24 h after transfer using FuGENE 6 (Roche) or Lipofectamine LTX (Invitrogen) as recommended by the manufacturer. Amino acid starvation was induced by washing cells twice with starvation buffer (140 mM NaCl, 1 mM $CaCl_2$, 1 mM $MgCl_2$, 5 mM glucose, 20 mM 4-(2-hydroxyethyl)-1-piperazineethanesulfonic acid [HEPES], pH 7.4), followed by a 6-h incubation with starvation buffer containing 1% (wt/vol) bovine serum albumin (BSA). Calcium phosphate precipitates were made by mixing 50 mM HEPES, pH 7.1, and 3 mM Na_2HPO_4 with an equal volume of 256 mM $CaCl_2$ just before adding this mixture to cultured cells at a final calcium concentration of 12.8 mM. Cells were then incubated for 4 h to induce macroautophagy. The FLAG-tagged Fis1 construct was purchased from Genecopeia (Rockville, MD). Fis1 siRNA oligonucleotides for coimmunoprecipitation experiments were from Sigma-Aldrich (ID SAS_Hs01_00171949_AS). These were transfected into HeLa cells with Oligofectamine as described (Head *et al.*, 2009). HA-tagged Drp1 was described previously (Smirnova *et al.*, 2001). Here we used an N- and C-terminal–tagged version. S600A and S600D mutants were made with a QuikChange protocol using *Dpn*I restriction enzyme and Phusion DNA polymerase from New England BioLabs (Ipswich, MA).

Mff$^{-/-}$ cells were made from HCT116 cells. The first allele was knocked out with rAAV-based homologous recombination (Topaloglu *et al.*, 2005) by targeting exon 4 (present in all Mff isoforms). Because targeting efficiency of rAAV was low (1.4%), transcription activator–like effector nucleases (TALENs) were used for the second allele of Mff (Miller *et al.*, 2011). A synthetic gene coding for Tale (+63) with N- and C-terminal regions of Tale, a half T repeat, and a FokI domain were cloned into the pcDNA3.1/Zeo (+) vector (Invitrogen) to make pcDNA-Talen (+63). An *Nhe*I site near the multiple cloning site of pcDNA3.1-Talen (+63) was removed by site-directed mutagenesis. The remaining *Nhe*I site was then used to clone the assembled left and right Tale repeats (Huang *et al.*, 2011), generating Mff-Talen-L and Mff-Talen-R constructs. The targeted sequence of Mff was GCTGTTCGCCAAAATGGACAGCTGGTCA-GAAATGATTCTCTGTGAGT. A donor DNA similar to that used for rAAV-based gene-targeting vector was constructed into pSEPT-puro vector (pSEPT vector with the neomycin marker replaced by puromycin). Lipofectamine LTX (Invitrogen) was used to transfect HCT116 cells with 0.1 µg of Mff-Talen-L, 0.1 µg of Mff-Talen-R, and 0.8 µg of donor DNA in a 12-well plate. One day after transfection, cells were transferred to 96-well plates with 0.4 µg/ml puromycin and grown for 10 d. Resistant clones were expanded and genotyped by PCR to ensure correct targeting. Cells were grown with McCoy's 5A medium, 10% fetal bovine serum, 1 mM glutamine, and nonessential amino acids.

Immunoblotting, immunostaining, and coimmunoprecipitation of mammalian cells

Total cell lysates were harvested for Western blot analysis by rinsing twice with phosphate buffered saline (PBS), followed by lysis with 2% (vol/vol) 3-[(3-cholamidopropyl)dimethylammonio]-1-propanesulfonate in PBS with protease inhibitor cocktail (Boehringer). The lysates were incubated for 30 min on ice and clarified by centrifugation (14,000 × *g* for 15 min at 4°C), and Laemmli sample buffer was added to the supernatants. From 30 to 60 µg of proteins was subjected to 4–12% Bis-Tris SDS–PAGE and transferred to polyvinylidene fluoride membranes. After blocking with 5% milk in PBS-Tween 20 (PBS-T) buffer, membranes were incubated with primary antibodies at room temperature. Membranes were washed three times with PBS-T and incubated with horseradish peroxidase–conjugated secondary antibodies (GE Healthcare, Little Chalfont, UK). Immunoreactive protein bands were detected by ECL Plus reagents (GE Healthcare) and analyzed with a ChemiDoc (BioRad, Hercules, CA). For immunostaining, cells were grown in dishes with borosilicate slides, fixed for 25 min with 4% paraformaldehyde in PBS, and permeabilized for 15 min with 0.15% (vol/vol) Triton X-100 in PBS. Cells were then blocked for 45 min with 10% BSA in PBS and incubated with primary antibodies. Secondary antibodies were Alexa Fluor 594– or 647–conjugated goat anti-mouse or rabbit IgG (Invitrogen). Mammalian cells were imaged with an LSM510 confocal microscope equipped with a 63×/1.4 NA Plan-Apochromat lens (Carl Zeiss). Images were processed with Photoshop.

For immuno–electron microscopy, HCT116 WT and Fis1$^{-/-}$ cells stably expressing YFP-LC3 and mCherry-Parkin were treated with valinomycin for 3 h and fixed for 30 min with 4% paraformaldehyde and 0.05% glutaraldehyde in PBS. The fixed cells were washed four times with PBS, followed by permeabilization for 40 min with 0.1% saponin and 5% goat serum in PBS. The cells were then incubated for 1 h with mouse anti-GFP antibody (clone 3E6 from Invitrogen), followed by 1 h with nanogold-conjugated anti-mouse IgG antibody

(Nanoprobes, Yaphank, NY) and further processing as described (Tanner *et al.*, 1996). Thin sections (~80 nm) were counterstained with uranyl acetate and lead citrate. The sections were examined with a JEOL 200 CX transmission electron microscope. Images were collected with a digital charge-coupled device camera (XR-100 CCD; AMT, Danvers, MA).

For coimmunoprecipitation, HeLa cells were grown in 10-cm dishes, transfected with FuGENE HD (Promega, Madison, WI), and harvested by scraping cells and washing them with PBS, followed by 30 min at 25°C with 1 mM DSP cross-linker (Pierce/Thermo, Rockford, IL) and quenching for 15 min on ice with 10 mM Tris-HCl, pH 7.5. Lysis was done with 1% SDS as described (Otera *et al.*, 2010) or with RIPA buffer. Cell lysates were sonicated for 10 s, followed by centrifugation for 15 min at 21,000 × *g*. The supernatant was incubated with immune-precipitating antibody and Protein G Dynabeads (Invitrogen). The control antibody was mouse normal IgG.

ACKNOWLEDGMENTS

We thank other members of the van der Bliek and Youle labs for helpful discussions. Strains were provided by the *Caenorhabditis* Genetics Center and S. Mitani. Technical support for electron microscopy was provided by the National Institute of Neurological Disorders and Stroke EM Facility. This work was supported by grants from the National Institutes of Health (GM051866) and the National Science Foundation (0552271) to A.M.V.D.B. B.P.H. received a National Institutes of Health Training Grant (T32-GM07104). S.K. was supported by a fellowship from the Naito Foundation and the Nakatomi Foundation. N.H. was supported by the Japan Society for the Promotion of Science, and K.Y. was supported by a Japan Society for the Promotion of Science Fellowship for Research Abroad.

REFERENCES

Alirol E, James D, Huber D, Marchetto A, Vergani L, Martinou JC, Scorrano L (2006). The mitochondrial fission protein hFis1 requires the endoplasmic reticulum gateway to induce apoptosis. Mol Biol Cell 17, 4593–4605.

Bleazard W, McCaffery JM, King EJ, Bale S, Mozdy A, Tieu Q, Nunnari J, Shaw JM (1999). The dynamin-related GTPase Dnm1 regulates mitochondrial fission in yeast. Nat Cell Biol 1, 298–304.

Breckenridge DG, Kang BH, Kokel D, Mitani S, Staehelin LA, Xue D (2008). *Caenorhabditis elegans* drp-1 and fis-2 regulate distinct cell-death execution pathways downstream of ced-3 and independent of ced-9. Mol Cell 31, 586–597.

Chan NC, Salazar AM, Pham AH, Sweredoski MJ, Kolawa NJ, Graham RL, Hess S, Chan DC (2011). Broad activation of the ubiquitin-proteasome system by Parkin is critical for mitophagy. Hum Mol Genet 20, 1726–1737.

Deng H, Dodson MW, Huang H, Guo M (2008). The Parkinson's disease genes pink1 and parkin promote mitochondrial fission and/or inhibit fusion in *Drosophila*. Proc Natl Acad Sci USA 105, 14503–14508.

Ding WX, Ni HM, Li M, Liao Y, Chen X, Stolz DB, Dorn GW2nd, Yin XM (2010). Nix is critical to two distinct phases of mitophagy, reactive oxygen species-mediated autophagy induction and Parkin-ubiquitin-p62-mediated mitochondrial priming. J Biol Chem 285, 27879–27890.

Frank M, Duvezin-Caubet S, Koob S, Occhipinti A, Jagasia R, Petcherski A, Ruonala MO, Priault M, Salin B, Reichert AS (2012). Mitophagy is triggered by mild oxidative stress in a mitochondrial fission dependent manner. Biochim Biophys Acta 1823, 2297–2310.

Friedman JR, Lackner LL, West M, DiBenedetto JR, Nunnari J, Voeltz GK (2011). ER tubules mark sites of mitochondrial division. Science 334, 358–362.

Gandre-Babbe S, van der Bliek AM (2008). The novel tail-anchored membrane protein Mff controls mitochondrial and peroxisomal fission in mammalian cells. Mol Biol Cell 19, 2402–2412.

Gao W, Ding WX, Stolz DB, Yin XM (2008). Induction of macroautophagy by exogenously introduced calcium. Autophagy 4, 754–761.

Gomes LC, Scorrano L (2008). High levels of Fis1, a pro-fission mitochondrial protein, trigger autophagy. Biochim Biophys Acta 1777, 860–866.

Griffin EE, Graumann J, Chan DC (2005). The WD40 protein Caf4p is a component of the mitochondrial fission machinery and recruits Dnm1p to mitochondria. J Cell Biol 170, 237–248.

Hamasaki M *et al.* (2013). Autophagosomes form at ER-mitochondria contact sites. Nature 495, 389–393.

Han XJ, Lu YF, Li SA, Kaitsuka T, Sato Y, Tomizawa K, Nairn AC, Takei K, Matsui H, Matsushita M (2008). CaM kinase I alpha-induced phosphorylation of Drp1 regulates mitochondrial morphology. J Cell Biol 182, 573–585.

Haynes CM, Petrova K, Benedetti C, Yang Y, Ron D (2007). ClpP mediates activation of a mitochondrial unfolded protein response in *C. elegans*. Dev Cell 13, 467–480.

Head B, Griparic L, Amiri M, Gandre-Babbe S, van der Bliek AM (2009). Inducible proteolytic inactivation of OPA1 mediated by the OMA1 protease in mammalian cells. J Cell Biol 187, 959–966.

Head BP, Zulaika M, Ryazantsev S, van der Bliek AM (2011). A novel mitochondrial outer membrane protein, MOMA-1, that affects cristae morphology in *Caenorhabditis elegans*. Mol Biol Cell 22, 831–841.

Huang P, Xiao A, Zhou M, Zhu Z, Lin S, Zhang B (2011). Heritable gene targeting in zebrafish using customized TALENs. Nat Biotechnol 29, 699–700.

Ingerman E, Perkins EM, Marino M, Mears JA, McCaffery JM, Hinshaw JE, Nunnari J (2005). Dnm1 forms spirals that are structurally tailored to fit mitochondria. J Cell Biol 170, 1021–1027.

Iwasawa R, Mahul-Mellier AL, Datler C, Pazarentzos E, Grimm S (2011). Fis1 and Bap31 bridge the mitochondria-ER interface to establish a platform for apoptosis induction. EMBO J 30, 556–568.

James DI, Parone PA, Mattenberger Y, Martinou JC (2003). hFis1, a novel component of the mammalian mitochondrial fission machinery. J Biol Chem 278, 36373–36379.

Jofuku A, Ishihara N, Mihara K (2005). Analysis of functional domains of rat mitochondrial Fis1, the mitochondrial fission-stimulating protein. Biochem Biophys Res Commun 333, 650–659.

Kim H, Scimia MC, Wilkinson D, Trelles RD, Wood MR, Bowtell D, Dillin A, Mercola M, Ronai ZA (2011). Fine-tuning of Drp1/Fis1 availability by AKAP121/Siah2 regulates mitochondrial adaptation to hypoxia. Mol Cell 44, 532–544.

Kobayashi S, Tanaka A, Fujiki Y (2007). Fis1, DLP1, and Pex11p coordinately regulate peroxisome morphogenesis. Exp Cell Res 313, 1675–1686.

Koch A, Yoon Y, Bonekamp NA, McNiven MA, Schrader M (2005). A role for Fis1 in both mitochondrial and peroxisomal fission in mammalian cells. Mol Biol Cell 16, 5077–5086.

Koirala S, Bui HT, Schubert HL, Eckert DM, Hill CP, Kay MS, Shaw JM (2010). Molecular architecture of a dynamin adaptor: implications for assembly of mitochondrial fission complexes. J Cell Biol 191, 1127–1139.

Koirala S, Guo Q, Kalia R, Bui HT, Eckert DM, Frost A, Shaw JM (2013). Interchangeable adaptors regulate mitochondrial dynamin assembly for membrane scission. Proc Natl Acad Sci USA 110, E1342–E1351.

Korobova F, Ramabhadran V, Higgs HN (2013). An actin-dependent step in mitochondrial fission mediated by the ER-associated formin INF2. Science 339, 464–467.

Labrousse AM, Zapaterra M, Rube DA, van der Bliek AM (1999). *C. elegans* dynamin-related protein *drp-1* controls severing of the mitochondrial outer membrane. Mol Cell 4, 815–826.

Lee YJ, Jeong SY, Karbowski M, Smith CL, Youle RJ (2004). Roles of the mammalian mitochondrial fission and fusion mediators Fis1, Drp1, and Opa1 in apoptosis. Mol Biol Cell 15, 5001–5011.

Loson OC, Song Z, Chen H, Chan DC (2013). Fis1, Mff, MiD49, and MiD51 mediate Drp1 recruitment in mitochondrial fission. Mol Biol Cell 24, 659–667.

Melendez A, Talloczy Z, Seaman M, Eskelinen EL, Hall DH, Levine B (2003). Autophagy genes are essential for dauer development and life-span extension in *C. elegans*. Science 301, 1387–1391.

Miller JC *et al.* (2011). A TALE nuclease architecture for efficient genome editing. Nat Biotechnol 29, 143–148.

Montessuit S *et al.* (2010). Membrane remodeling induced by the dynamin-related protein Drp1 stimulates Bax oligomerization. Cell 142, 889–901.

Mozdy AD, McCaffery JM, Shaw JM (2000). Dnm1p GTPase-mediated mitochondrial fission is a multi-step process requiring the novel integral membrane component Fis1p. J Cell Biol 151, 367–380.

Myhill N, Lynes EM, Nanji JA, Blagoveshchenskaya AD, Fei H, Carmine Simmen K, Cooper TJ, Thomas G, Simmen T (2008). The subcellular distribution of calnexin is mediated by PACS-2. Mol Biol Cell 19, 2777–2788.

Narendra D, Tanaka A, Suen DF, Youle RJ (2008). Parkin is recruited selectively to impaired mitochondria and promotes their autophagy. J Cell Biol 183, 795–803.
Onoue K *et al.* (2013). Fis1 acts as a mitochondrial recruitment factor for TBC1D15 that is involved in regulation of mitochondrial morphology. J Cell Sci 126, 176–185.
Otera H, Wang C, Cleland MM, Setoguchi K, Yokota S, Youle RJ, Mihara K (2010). Mff is an essential factor for mitochondrial recruitment of Drp1 during mitochondrial fission in mammalian cells. J Cell Biol 191, 1141–1158.
Palmer CS, Elgass KD, Parton RG, Osellame LD, Stojanovski D, Ryan MT (2013). MiD49 and MiD51 can act independently of Mff and Fis1 in Drp1 recruitment and are specific for mitochondrial fission. J Biol Chem 288, 27584–27593.
Palmer CS, Osellame LD, Laine D, Koutsopoulos OS, Frazier AE, Ryan MT (2011). MiD49 and MiD51, new components of the mitochondrial fission machinery. EMBO Rep 12, 565–573.
Panowski SH, Wolff S, Aguilaniu H, Durieux J, Dillin A (2007). PHA-4/Foxa mediates diet-restriction-induced longevity of *C. elegans*. Nature 447, 550–555.
Poole AC, Thomas RE, Andrews LA, McBride HM, Whitworth AJ, Pallanck LJ (2008). The PINK1/Parkin pathway regulates mitochondrial morphology. Proc Natl Acad Sci USA 105, 1638–1643.
Qi X, Disatnik MH, Shen N, Sobel RA, Mochly-Rosen D (2011). Aberrant mitochondrial fission in neurons induced by protein kinase Cδ under oxidative stress conditions in vivo. Mol Biol Cell 22, 256–265.
Rakovic A, Grunewald A, Seibler P, Ramirez A, Kock N, Orolicki S, Lohmann K, Klein C (2010). Effect of endogenous mutant and wild-type PINK1 on Parkin in fibroblasts from Parkinson disease patients. Hum Mol Genet 19, 3124–3137.
Sarraf SA, Raman M, Guarani-Pereira V, Sowa ME, Huttlin EL, Gygi SP, Harper JW (2013). Landscape of the Parkin-dependent ubiquitylome in response to mitochondrial depolarization. Nature 496, 372–376.
Smirnova E, Griparic L, Shurland DL, van der Bliek AM (2001). Dynamin-related protein Drp1 is required for mitochondrial division in mammalian cells. Mol Biol Cell 12, 2245–2256.
Taguchi N, Ishihara N, Jofuku A, Oka T, Mihara K (2007). Mitotic phosphorylation of dynamin-related GTPase Drp1 participates in mitochondrial fission. J Biol Chem 282, 11521–11529.
Tanaka A, Cleland MM, Xu S, Narendra DP, Suen DF, Karbowski M, Youle RJ (2010). Proteasome and p97 mediate mitophagy and degradation of mitofusins induced by Parkin. J Cell Biol 191, 1367–1380.
Tanner VA, Ploug T, Tao-Cheng JH (1996). Subcellular localization of SV2 and other secretory vesicle components in PC12 cells by an efficient method of preembedding EM immunocytochemistry for cell cultures. J Histochem Cytochem 44, 1481–1488.
Tieu Q, Nunnari J (2000). Mdv1p is a WD repeat protein that interacts with the dynamin-related GTPase, Dnm1p, to trigger mitochondrial division. J Cell Biol 151, 353–366.
Timmons L, Court DL, Fire A (2001). Ingestion of bacterially expressed dsRNAs can produce specific and potent genetic interference in *Caenorhabditis elegans*. Gene 263, 103–112.
Topaloglu O, Hurley PJ, Yildirim O, Civin CI, Bunz F (2005). Improved methods for the generation of human gene knockout and knockin cell lines. Nucleic Acids Res 33, e158.
Twig G *et al.* (2008). Fission and selective fusion govern mitochondrial segregation and elimination by autophagy. EMBO J 27, 433–446.
Wang W, Wang Y, Long J, Wang J, Haudek SB, Overbeek P, Chang BH, Schumacker PT, Danesh FR (2012). Mitochondrial fission triggered by hyperglycemia is mediated by ROCK1 activation in podocytes and endothelial cells. Cell Metab 15, 186–200.
Yamamoto A, Tagawa Y, Yoshimori T, Moriyama Y, Masaki R, Tashiro Y (1998). Bafilomycin A1 prevents maturation of autophagic vacuoles by inhibiting fusion between autophagosomes and lysosomes in rat hepatoma cell line, H-4-II-E cells. Cell Struct Funct 23, 33–42.
Yang Y, Ouyang Y, Yang L, Beal MF, McQuibban A, Vogel H, Lu B (2008). Pink1 regulates mitochondrial dynamics through interaction with the fission/fusion machinery. Proc Natl Acad Sci USA 105, 7070–7075.
Yoon Y, Krueger EW, Oswald BJ, McNiven MA (2003). The mitochondrial protein hFis1 regulates mitochondrial fission in mammalian cells through an interaction with the dynamin-like protein DLP1. Mol Cell Biol 23, 5409–5420.
Yoshii SR, Kishi C, Ishihara N, Mizushima N (2011). Parkin mediates proteasome-dependent protein degradation and rupture of the outer mitochondrial membrane. J Biol Chem 286, 19630–19640.
Youle RJ, Narendra DP (2011). Mechanisms of mitophagy. Nat Rev Mol Cell Biol 12, 9–14.
Zhao J, Liu T, Jin S, Wang X, Qu M, Uhlen P, Tomilin N, Shupliakov O, Lendahl U, Nister M (2011). Human MIEF1 recruits Drp1 to mitochondrial outer membranes and promotes mitochondrial fusion rather than fission. EMBO J 30, 2762–2778.

OPEN ACCESS Freely available online

PLOS | ONE

Large-Scale RNA Interference Screening in Mammalian Cells Identifies Novel Regulators of Mutant Huntingtin Aggregation

Tomoyuki Yamanaka[1,2,3,6☯], Hon Kit Wong[2,4☯], Asako Tosaki[2], Peter O. Bauer[2], Koji Wada[2], Masaru Kurosawa[1,2,3,6], Tomomi Shimogori[3], Nobutaka Hattori[5], Nobuyuki Nukina[1,2,3,6]*

1 Department of Neuroscience for Neurodegenerative Disorders, Juntendo University Graduate School of Medicine, Tokyo, Japan, **2** Laboratory for Structural Neuropathology, RIKEN Brain Science Institute, Saitama, Japan, **3** Laboratory for Molecular Mechanisms of Thalamus Development, RIKEN Brain Science Institute, Saitama, Japan, **4** Center for Neurologic Diseases, Department of Neurology, Brigham and Women's Hospital and Harvard Medical School, Harvard Institutes of Medicine, Boston, Massachusetts, United States of America, **5** Department of Neurology, Juntendo University Graduate School of Medicine, Tokyo, Japan, **6** CREST (Core Research for Evolutionary Science and Technology), JST, Tokyo, Japan

Abstract

In polyglutamine (polyQ) diseases including Huntington's disease (HD), mutant proteins containing expanded polyQ stretch form aggregates in neurons. Genetic or RNAi screenings in yeast, *C. elegans* or *Drosophila* have identified multiple genes modifying polyQ aggregation, a few of which are confirmed effective in mammals. However, the overall molecular mechanism underlying polyQ protein aggregation in mammalian cells still remains obscure. We here perform RNAi screening in mouse neuro2a cells to identify mammalian modifiers for aggregation of mutant huntingtin, a causative protein of HD. By systematic cell transfection and automated cell image analysis, we screen ~12000 shRNA clones and identify 111 shRNAs that either suppress or enhance mutant huntingtin aggregation, without altering its gene expression. Classification of the shRNA-targets suggests that genes with various cellular functions such as gene transcription and protein phosphorylation are involved in modifying the aggregation. Subsequent analysis suggests that, in addition to the aggregation-modifiers sensitive to proteasome inhibition, some of them, such as a transcription factor Tcf20, and kinases Csnk1d and Pik3c2a, are insensitive to it. As for Tcf20, which contains polyQ stretches at N-terminus, its binding to mutant huntingtin aggregates is observed in neuro2a cells and in HD model mouse neurons. Notably, except Pik3c2a, the rest of the modifiers identified here are novel. Thus, our first large-scale RNAi screening in mammalian system identifies previously undescribed genetic players that regulate mutant huntingtin aggregation by several, possibly mammalian-specific mechanisms.

Citation: Yamanaka T, Wong HK, Tosaki A, Bauer PO, Wada K, et al. (2014) Large-Scale RNA Interference Screening in Mammalian Cells Identifies Novel Regulators of Mutant Huntingtin Aggregation. PLoS ONE 9(4): e93891. doi:10.1371/journal.pone.0093891

Editor: Yoshitaka Nagai, National Center of Neurology and Psychiatry, Japan

Received August 19, 2013; **Accepted** March 10, 2014; **Published** April 4, 2014

Copyright: © 2014 Yamanaka et al. This is an open-access article distributed under the terms of the Creative Commons Attribution License, which permits unrestricted use, distribution, and reproduction in any medium, provided the original author and source are credited.

Funding: This work was supported by a Grant-in-Aid from Ministry of Education, Culture, Sports, Science and Technology (MEXT) of Japan for TY (24111553, 23700430) and NN (22110004, 22240037, 24659436); by Life Science Foundation of Japan for TY; by Mochida Memorial Foundation for Medical and Pharmaceutical Research for TY; by CREST from JST for NN; and by Grant-in-Aid for the Research on Measures for Ataxic Diseases from the Ministry of Health, Welfare and Labor for NN. The funders had no role in study design, data collection and analysis, decision to publish, or preparation of the manuscript.

Competing Interests: The authors have declared that no competing interests exist.

* E-mail: nnukina@juntendo.ac.jp

☯ These authors contributed equally to this work.

Introduction

Polyglutamine (polyQ) diseases are adult-onset hereditary neurodegenerative disorders. These include Huntington's disease (HD), spinocerebellar ataxias (SCA1, 2, 3, 6, 7, 17), dentatorubral-pallidoluysian atrophy (DRPLA) and spinobulbar muscular atrophy (SBMA). The polyQ diseases are caused by expansion of CAG repeats in certain causative genes. The mutant proteins containing expanded polyQ stretch are misfolded and aggregated, leading to formation of nuclear inclusions in neurons [1,2].

The polyQ protein aggregation accompanies sequestration of several cellular components such as transcription factors [3–7] and RNA binding proteins [8,9], leading to dysregulation of gene expression during neurodegeneration [10–12]. In addition, polyQ-mediated cell toxicity is reported to be reduced through suppressing polyQ aggregation by chaperones [13–18], chaperonin [19–21], QBP1 (polyQ-binding peptide 1) [22,23], or chemical compounds such as Congo Red [24] or trehalose [25]. Thus, examination of molecular mechanisms underlying polyQ aggregation is one of the effective strategies for understanding pathomechanism of and searching therapeutic targets for polyQ diseases.

In past 10 years, several groups have performed genetic or RNA interference (RNAi) screening to identify polyQ aggregation-modifying genes using yeast [26], *C. elegans* [27–30] or *Drosophila* models [31–34]. These screenings have identified genes in various contexts such as transcription, RNA processing, protein transport and signal transduction, in addition to protein folding and degradation. These observations suggest that multiple cellular pathways are involved in the regulation of polyQ protein aggregation in non-mammalian systems. Although a few of their orthologues are shown to modify polyQ protein aggregation in

mammalian cells [26,34], a large-scale, systematic screen has not been performed in any mammalian systems and the overall molecular mechanism underlying polyQ protein aggregation in mammalian cells remains obscure.

To this end, we perform RNAi screening in mouse neuroblastoma cells to attempt to identify novel aggregation-modifiers for mutant huntingtin (Htt), a causative protein of HD, in mammals. To the best of our knowledge, this is the first comprehensive analysis of polyQ aggregation-modifying genes in mammals. We transduce ~12000 short hairpin RNA (shRNA) clones into neuro2a cells that inducibly express mutant Htt, and analyze the aggregation by automated quantitative fluorescence microscopy. After three screenings, we identify 111 shRNAs that specifically modify the mutant Htt aggregation in neuro2a cells. Subsequent analyses suggest that the modifications can be mediated by several mechanisms, that is, by direct/indirect regulation through proteasome-dependent/-independent pathways. Importantly, all of the shRNA targets except of one gene [33] are not found by previous screenings using other organisms described above. Thus, our RNAi screening identifies previously undescribed genes involved in mutant Htt aggregation in mammalian cells.

Results

Identification of shRNAs that modify mutant Nhtt aggregation in neuro2a cells

To identify modifiers of mutant Htt aggregation in mammalian cells, we performed shRNA screening using mouse neuro2a cells that inducibly expressed exon 1 of Htt (Nhtt) containing a 150Q tagged with an EGFP at its C-terminus (Nhtt150Q-EGFP), under the control of ponasterone A [35]. shRNA libraries were purchased from Open Biosystems, in which shRNA clones were supplied as *E. coli* glycerol stocks in 96 well plate-formats. We used total 122 plates for plasmid DNA purification and obtained 11346 shRNA clones with transfection grade DNA. Scheme of experimental procedure is outlined in Figure 1. First, neuro2a cells were seeded on 96 well plates and transiently transfected with shRNA clones. Cells were then differentiated by dibutyryl cyclic AMP (dcAMP) on the same day and selected with puromycin on the next day. After the selection, they were treated with ponasterone A to induce Nhtt150Q-EGFP expression. EGFP positive aggregates will be allowed to form for one day. After fixation and nuclear staining with DAPI or Hoechst, the number of aggregates-containing cells and total number of cells were automatically quantified by Cellomics ArrayScan HCS Reader, a cell image analyzer equipped with fluorescence microscopy.

The screening strategy is summarized in Figure 2. In the first screening, we screened 11346 shRNA clones based on the z score (mean z score is <-1.5 or >1.5) and finally obtained 602 shRNAs that were able to modify Nht150Q-EGFP aggregation in neuro2a cells (Figure 3A). To exclude the shRNAs that modify the aggregation purely acting on Nhtt expression itself, we performed a second screen, in which we used neuro2a cells expressing non-aggregating Nhtt16Q-EGFP [35]. After transfection and induction of Nhtt16Q-EGFP expression as above, EGFP intensities in the cells were quantified by ArrayScan reader. Through this analysis, we noticed that the shRNAs that induced Nhtt16Q-EGFP expression were relatively enriched in the aggregation-enhancing shRNAs (Figure 3B), suggesting that their enhancing effect was just caused by inducing Nhtt expression. After the second screen, 270 shRNAs were remained as candidates as they did not show significant alteration in Nhtt16Q-EGFP expression (Figure 3B). To obtain shRNAs that reproducibly modifying aggregation, we again used Nhtt150Q-EGFP cells for the third screening. Finally, we obtained 111 shRNAs that specifically and reproducibly modified Nhtt150Q-EGFP aggregation in neuro2a cells (Figure 3C).

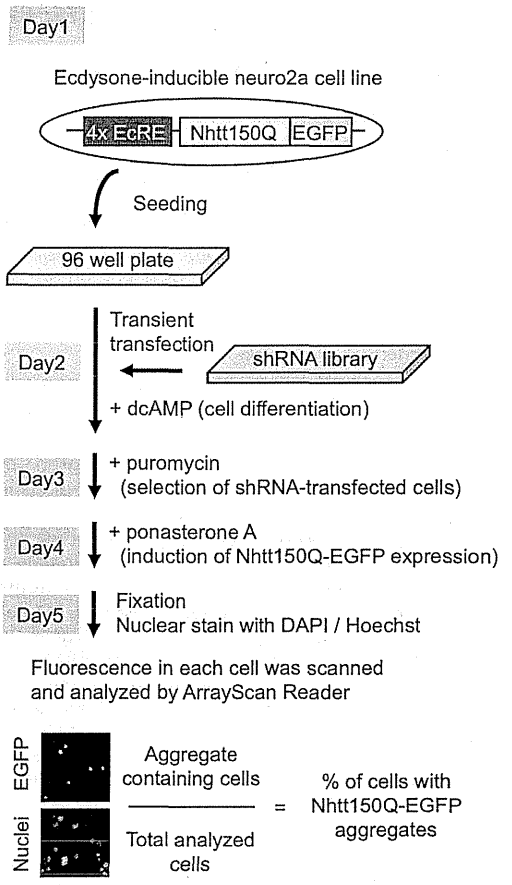

Figure 1. Experimental procedure of screening of shRNAs that modify Nhtt150Q-EGFP aggregation in neuro2a cells. Neuro2a cells inducibly expressing Nhtt150Q-EGFP under ecdysone-responsive element (EcRE) were seeded on a 96 well culture plate. On the next day, the cells were transiently transfected with shRNAs prepared from shRNA library plates. The cells were then differentiated by dcAMP on the same day and selected with puromycin on the next day, after which they were treated with ponasterone A to induce Nhtt150Q-EGFP expression. After 24 hr, the cells were fixed with 4% PFA and incubated with DAPI or Hoechst for nuclear staining. Fluorescence cell images were automatically obtained and analyzed by ArrayScan HCS Reader, and percent of cells with Nhtt150Q-EGFP aggregates among total analyzed cells was calculated.
doi:10.1371/journal.pone.0093891.g001

Validation, classification and proteasome-dependency of the aggregation-modification by the identified shRNAs

Among the final 111 shRNAs, 63 suppressed and 48 enhanced the aggregation of mutant Nhtt (Table 1, 2) (complete screening data for 111 candidates are described in Data S1). Figure 3D shows representative cell images of the aggregation-modification by the shRNAs; Atf3 or Ppt2 shRNAs reduced Nhtt-150QEGFP aggregates compared with non-silencing control whereas Cish or Gnai2 shRNAs increased them. To validate the gene-knockdown effect by the shRNAs, we designed other RNAi sequences (Inv-1 and -2) by Invitrogen's BLOCK-iT RNAi Designer for some of the genes (Data S2), and expressed as miRNA (miR RNAi) using

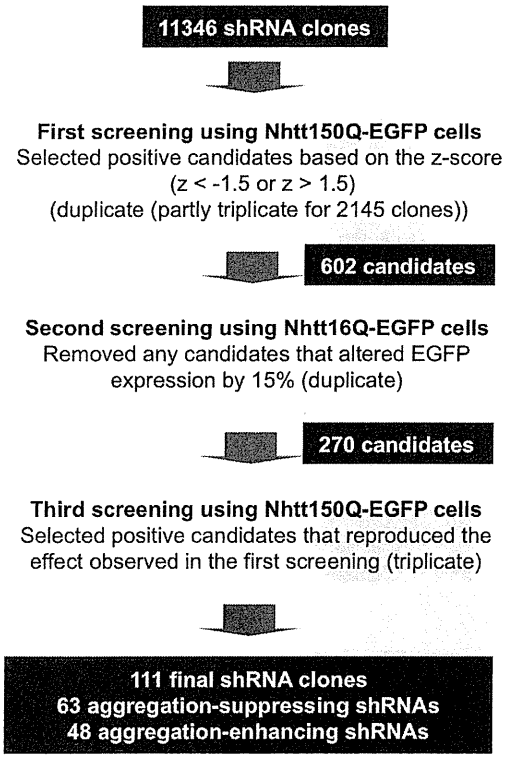

Figure 2. Summary of the shRNA screening. Total 11346 shRNA clones were subjected to the first screening using Nhtt150Q-EGFP cells. The screening was performed in duplicate (partly in triplicate), and shRNAs altering Nhtt150Q-EGFP aggregation at <-1.5 or >1.5 of z-score were selected as positive candidates. Obtained 602 clones were then subjected to the second screening using Nhtt16Q-EGFP cells to exclude the shRNAs modifying the aggregation by altering Nhtt expression itself. shRNAs altering EGFP intensity by 15% compared with the control were removed. Remaining 270 candidates were subjected to the third screening using Nhtt150Q-EGFP cells for confirmation (triplicate). We performed statistical analysis (t-test) in the third screening and shRNAs with $P<0.1$ were included as candidates. Finally, 111 shRNAs were obtained, among which 63 shRNAs suppressed and 48 shRNAs enhanced the Nhtt150Q-EGFP aggregation.
doi:10.1371/journal.pone.0093891.g002

pcDNA6.2-mRFP-miR vector [36]. We reproduced the aggregation-modifying ability in 12 out of 15 genes (80%) by at least one of the miRNAs (Figure 3E), supporting the validity of our screening strategy and results.

To examine the molecular mechanism underlying mutant Nhtt aggregation by these shRNAs, we classified the final 111 shRNA-target genes using PANTHER Classification System [37]. When focused on molecular function, they were classified into various functions such as catalytic, receptor and transcription regulator activities (Figure 4A). Classification by PANTHER protein class also suggests the genes with various activities involved in mutant Nhtt aggregation (Figure 4B). Another Classification method further suggests the involvement of multiple biological processes in the aggregation modification (Figure 4C). Although no marked difference was observed between the target genes of the aggregation-suppressing and -enhancing shRNAs, transcription factors such as Atf3 and Tcf20 was more abundant in the suppressors' targets (12.7%; 8 out of 63) than the enhancers' targets (4.1%; 2 out of 48) (Figure 4A, B). In contrast, genes for membrane trafficking such as Stxbp1 and Snx10 were only found in the enhancers' targets (8.3%; 4 out of 48) (Figure 4B). We also performed Statistical Overrepresentation Test using PANTHER Classification System, however any of gene ontology (GO) term or pathway was not significantly enriched (data not shown). These data suggest that genes with broad molecular and biological functions modify the mutant Nhtt aggregation whereas some specific cellular functions such as gene transcription and membrane trafficking may be differentially involved in the modification.

Several lines of studies have suggested an involvement of ubiquitin-proteasome system, a major protein degradation system in cells, in mutant Htt degradation [34,38–41]. In addition, another degradation system, autophagy, is also recently shown to be involved in clearance mutant Htt aggregates [36,42–45]. To examine whether the aggregation-modification by identified shRNAs involves these systems, we picked up 10 aggregation-suppressing shRNAs whose targets have various molecular and biological functions (Figure 4), and examined their effect in the presence of MG132 or bafilomycin A1 (Baf A1), inhibitor of proteasome or autophagy, respectively. We found that MG132 but not Baf A1 relieved the aggregation-suppressing effect of several shRNAs, such as those for Atf3, Cradd, Tmem179b and Pdcd4 (Figure 5), suggesting that these genes modify the mutant Nhtt aggregation through proteasome-dependent mechanism.

Tcf20 binds to mutant Nhtt aggregates in neuro2a cells and R6/2 mouse brain neurons

In addition to the genes whose shRNAs' effect was sensitive to MG132 as described above, we found several genes including Ppt2 and Tcf20 whose shRNAs' effect was insensitive to it (Figure 5), suggesting proteasome-independent modification by these genes. Among them, we focused on Tcf20 because it is relatively Q-rich (Q composition is 9.7%) among the identified modifiers (mean Q composition is $4.59\pm1.92\%$) and notably it contains several polyQ stretches in the N-terminal region (Figure 6A). Because some of Q-rich proteins are shown to directly co-aggregate with mutant Htt [3–6,8,9], it is possible that Tcf20 directly interacts with mutant Nhtt aggregates.

To examine this possibility, we cloned Tcf20 cDNA into pcDNA-DEST40 vector with a V5 tag at its C-terminus, and expressed Tcf20-V5 in neuro2a cells together with Nhtt150Q-EGFP-NLS (nuclear localization signal). As shown in Figure 6B, Tcf20-V5 was clearly co-localized with Nhtt150Q-EGFP-NLS aggregates, whereas it was only diffusely localized in the nucleus in the cells without the aggregates. Tcf20-V5 was also co-localized with cytoplasmic Nhtt150Q-EGFP aggregates (Figure 6C). In contrast, these co-localization was not observed for LacZ or other potential modifiers without polyQ-stretch such as Rab2b and Ddr2 (Q compositions are 5.6% and 4.0%, respectively) (Figure 6C; Ddr2, data not shown). We further found that Tcf20 N-terminal constructs (1~400 and 1~500) containing polyQ stretches preferentially co-localized with Nhtt150Q-EGFP aggregates (Figure 6C). In addition, these were insolubilized with Nhtt150Q-EGFP but not with Nhtt16Q-EGFP (Figure 6D), similar to a known aggregates-interacting protein, NF-YA [5]. Interestingly, overexpression of either N-terminal (1~400 and 1~500) or full-length of Tcf20 suppressed Nhtt150Q-EGFP aggregation (Figure 6E), suggesting that the Tcf20 interaction through its N-terminus suppresses mutant Nhtt aggregation when overexpressed. Finally, an antibody against Tcf20 stained puncta positive for Htt and Ub in cortical neurons of HD model mouse (Figure 7A, B), suggesting *in vivo* incorporation of Tcf20 into

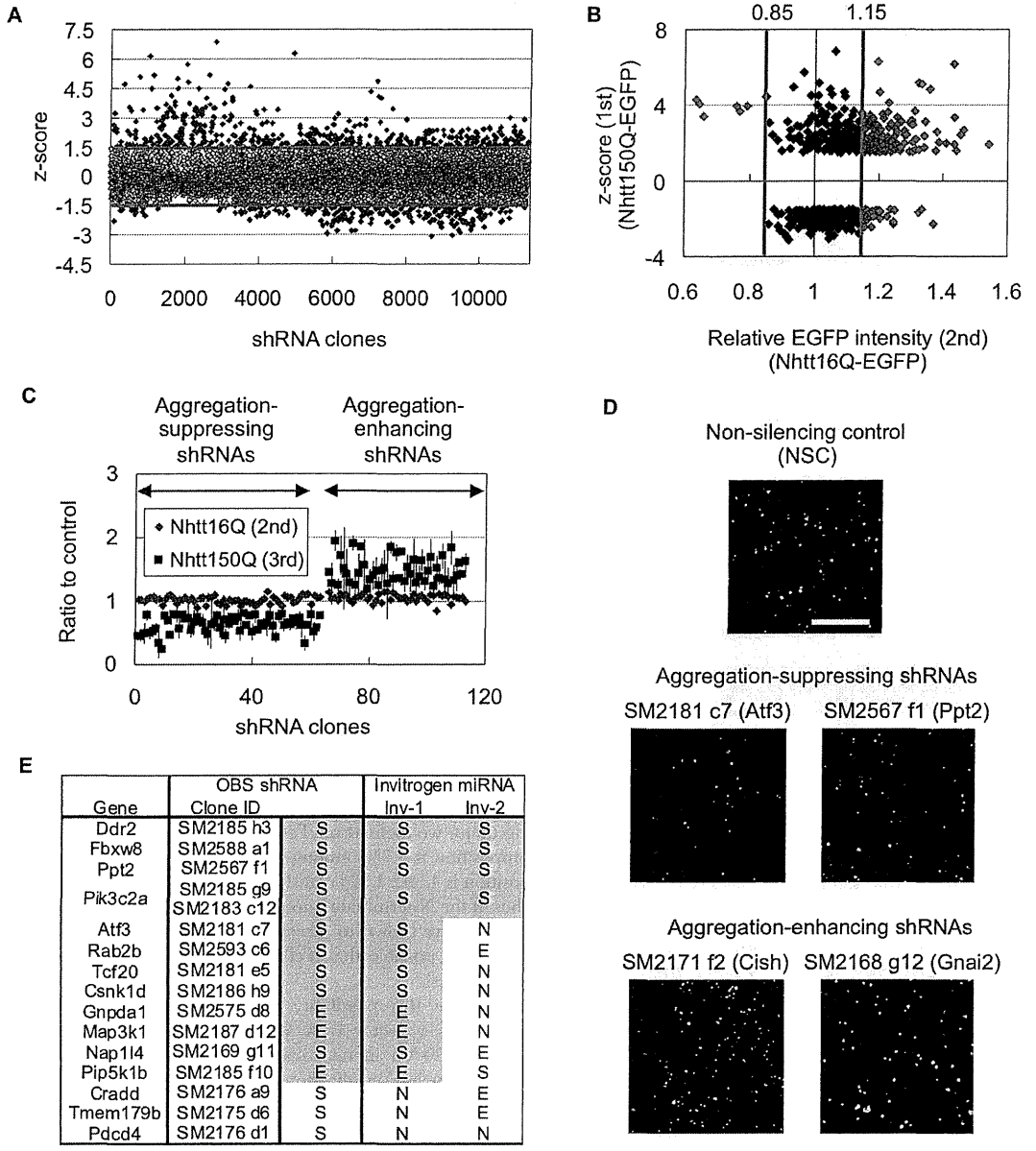

E

Gene	OBS shRNA Clone ID		Invitrogen miRNA Inv-1	Inv-2
Ddr2	SM2185 h3	S	S	S
Fbxw8	SM2588 a1	S	S	S
Ppt2	SM2567 f1	S	S	S
Pik3c2a	SM2185 g9	S	S	S
	SM2183 c12	S		
Atf3	SM2181 c7	S	S	N
Rab2b	SM2593 c6	S	S	E
Tcf20	SM2181 e5	S	S	N
Csnk1d	SM2186 h9	S	S	N
Gnpda1	SM2575 d8	E	E	N
Map3k1	SM2187 d12	E	E	N
Nap1l4	SM2169 g11	S	S	E
Pip5k1b	SM2185 f10	E	E	S
Cradd	SM2176 a9	S	N	E
Tmem179b	SM2175 d6	S	N	E
Pdcd4	SM2176 d1	S	N	N

Figure 3. Identification and validation of the shRNAs modifying Nhtt150Q-EGFP aggregation in neuro2a cells. (A) Summarized data of the first screening using Nhtt150Q-EGFP cells. Mean z-score of 11346 shRNA clones were plotted. shRNAs showing the z-score outside the range of ±1.5 were picked up as positive candidates (indicated as blue plots). (B) Summarized data of the second screening using Nhtt16Q-EGFP cells. The data (relative EGFP intensity; x-axis) were plotted against the first screening data (z-score; y-axis) for 602 shRNA clones. The shRNAs showing the EGFP intensity within 15% to the control were picked up as positive candidates (indicated as blue plots). (C) Data of the second and third screening for final 111 shRNA candidates. 63 shRNAs suppressed and 48 shRNAs enhanced the Nhtt150Q-EGFP aggregation without distinct alteration of Nhtt16Q-EGFP expression. (D) Example cell images. Two shRNAs targeting Atf3 or Ppt2 reduced the cells with Nhtt150Q-EGFP aggregates compared with non-silencing control whereas two shRNAs targeting Cish or Gnaj2 increased them. Bar is 0.2 mm. (E) Validation of the effect of Open Biosystems (OBS) shRNA by two miRNAs (Inv-1 and -2) binding to different sequences of the genes (Data S2). The S, N and E mean suppression, no-effect and enhancement for the Nhtt150Q-EGFP aggregation, respectively. In case of Pik3c2a, two different shRNAs were obtained. Note that the shRNA's effect was reproduced by at least one miRNA in 12 genes (80% of analyzed genes).
doi:10.1371/journal.pone.0093891.g003

inclusions containing mutant Nhtt aggregates. These data suggest that the Tcf20 specifically interacts with mutant Nhtt aggregates through its N-terminus containing polyQ stretches to be incorporated into the inclusion. Because both knockdown and overexpression showed suppressive effect on mutant Nhtt aggregation, moderate expression of Tcf20 might be appropriate for efficient aggregation. Alternatively, its direct interaction and transcriptional activity could be differentially involved in the regulation of mutant Nhtt aggregation.

Table 1. shRNAs suppressing Nhtt150Q aggregation in neuro2a cells.

	shRNA		1st (150Q)	2nd (16Q)	3rd (150Q)	
No	Clone ID	Gene	z-score	Ratio	Ratio (+ SD)	Gene Description
1	SM2173 d5	1810032O08Rik	−1.79	1.03	0.447 (+0.084)	RIKEN cDNA 1810032O08 gene
2	SM2177 c4	4933425L06Rik	−2.17	1.02	0.447 (+0.160)	RIKEN cDNA 4933425L06 gene
3	SM2179 b7	Abat	−1.65	0.99	0.493 (+0.086)	4-aminobutyrate aminotransferase
4	SM2574 c8	Aktip	−1.60	1.03	0.787 (+0.090)	thymoma viral proto-oncogene 1 interacting protein
5	SM2181 c7	Atf3	−1.51	1.06	0.499 (+0.093)	activating transcription factor 3
6	SM2172 b5	Birc6	−2.29	1.07	0.533 (+0.098)	baculoviral IAP repeat-containing 6
7	SM2173 f4	Casp3	−1.52	1.02	0.563 (+0.237)	caspase 3
8	SM2174 e3	Cd24a	−2.45	1.03	0.339 (+0.066)	CD24a antigen
9	SM2176 a9	Cradd	−2.27	0.93	0.241 (+0.028)	death domain-containing protein, RAIDD
10	SM2186 h9	Csnk1d	−2.22	1.03	0.771 (+0.060)	casein kinase 1, delta
11	SM2185 h3	Ddr2	−1.52	1.09	0.699 (+0.069)	discoidin domain receptor family, member 2
12	SM2168 c8	Ddx6	−1.75	1.10	0.467 (+0.038)	DEAD (Asp-Glu-Ala-Asp) box polypeptide 6
13	SM2579 f9	Efhb	−2.60	1.05	0.793 (+0.122)	EF hand domain family, member B
14	SM2558 e11	Enah	−1.55	0.96	0.787 (+0.148)	enabled homolog (Drosophila)
15	SM2588 a1	Fbxw8	−1.57	1.03	0.564 (+0.056)	F-box and WD-40 domain protein 8
16	SM2561 e3	Fcgr3	−1.90	1.02	0.781 (+0.024)	Fc receptor, IgG, low affinity III
17	SM2176 h8	Fgd1	−1.92	1.06	0.719 (+0.200)	FYVE, RhoGEF and PH domain containing 1
18	SM2560 h6	Fkbp9	−2.34	1.01	0.736 (+0.117)	FK506 binding protein 9
19	SM2179 b5	Fsd1l	−1.62	1.04	0.548 (+0.199)	FSD1-like
20	SM2179 e8	Gaa	−2.25	0.99	0.664 (+0.095)	glucosidase, alpha, acid
21	SM2560 e6	Gjb2	−1.77	0.89	0.743 (+0.036)	gap junction protein, beta 2
22	SM2177 e1	Gpr37	−2.79	1.05	0.680 (+0.141)	G protein-coupled receptor 37
23	SM2588 f3	Grhpr	−2.14	1.07	0.654 (+0.129)	glyoxylate reductase/hydroxypyruvate reductase
24	SM2174 g6	Hoxd3	−1.96	0.92	0.527 (+0.167)	homeobox D3
25	SM2175 c6	Jagn1	−1.68	1.06	0.473 (+0.381)	jagunal homolog 1 (Drosophila)
26	SM2591 e6	Klhl7	−1.66	1.06	0.635 (+0.120)	kelch-like 7
27	SM2134 h10	LOC195242	−1.92	1.10	0.650 (+0.099)	
28	SM2112 g12	LOC195373	−1.59	0.98	0.763 (+0.150)	
29	SM2185 a7	Lrguk	−1.79	0.95	0.577 (+0.211)	leucine-rich repeats and GUK containing
30	SM2587 b3	Mab21l3	−1.67	1.03	0.702 (+0.115)	mab-21-like 3 (C. elegans)
31	SM2169 g11	Nap1l4	−1.57	0.92	0.455 (+0.072)	nucleosome assembly protein 1-like 4
32	SM2146 b6	Nlrp10	−1.54	1.02	0.641 (+0.058)	NLR family, pyrin domain containing 10
33	SM2575 b10	Notch4	−2.02	1.00	0.745 (+0.048)	notch 4
34	SM2176 f1	Olfr1339	−1.99	1.01	0.676 (+0.118)	olfactory receptor 1339
35	SM2008 a5	Olfr1451	−1.94	1.01	0.746 (+0.160)	olfactory receptor 1451
36	SM2174 c1	Olfr339	−2.96	0.92	0.526 (+0.062)	olfactory receptor 339
37	SM2142 b5	Olfr530	−1.89	0.99	0.808 (+0.042)	olfactory receptor 530
38	SM2588 f4	Olfr668	−2.65	1.00	0.623 (+0.049)	olfactory receptor 668
39	SM2562 d2	P2ry1	−1.94	0.97	0.764 (+0.136)	purinergic receptor P2Y, G-protein coupled 1
40	SM2176 d1	Pdcd4	−2.32	0.97	0.512 (+0.123)	programmed cell death 4
41	SM2575 a6	Pf4	−2.46	0.93	0.780 (+0.041)	platelet factor 4
42	SM2183 c12	Pik3c2a	−2.08	0.96	0.548 (+0.057)	PI 3-kinase, C2 domain containing, alpha
43	SM2185 g9	Pik3c2a	−1.99	1.01	0.637 (+0.043)	PI 3-kinase, C2 domain containing, alpha
44	SM2134 a11	Pkd1l3	−1.53	1.03	0.606 (+0.198)	polycystic kidney disease 1 like 3
45	SM2177 e5	Plec	−1.82	1.15	0.657 (+0.134)	plectin
46	SM2148 a11	Ppfia1	−1.58	0.95	0.775 (+0.107)	PTPRF, interacting protein (liprin), alpha 1
47	SM2567 f1	Ppt2	−2.15	1.06	0.605 (+0.093)	palmitoyl-protein thioesterase 2
48	SM2149 a9	Ptprn2	−2.03	1.02	0.434 (+0.103)	protein tyrosine phosphatase, receptor type, N2

Table 1. Cont.

	shRNA		1st (150Q)	2nd (16Q)	3rd (150Q)	
No	Clone ID	Gene	z-score	Ratio	Ratio (+ SD)	Gene Description
49	SM2593 c6	Rab2b	−2.36	0.97	0.754 (+0.076)	RAB2B, member RAS oncogene family
50	SM2567 a8	Racgap1	−2.34	0.93	0.789 (+0.079)	Rac GTPase-activating protein 1
51	SM2008 h8	Rfc1	−1.65	1.09	0.614 (+0.074)	replication factor C (activator 1) 1
52	SM2588 d5	Rps27l	−1.58	1.06	0.660 (+0.087)	ribosomal protein S27-like
53	SM2169 b7	Slc25a14	−1.96	1.07	0.630 (+0.039)	solute carrier family 25member 14
54	SM2558 f9	Stfa3	−1.99	0.97	0.717 (+0.104)	stefin A3
55	SM2591 c7	Taf7l	−1.64	0.99	0.659 (+0.101)	TAF7-like RNA polymerase II, TBP-associated factor
56	SM2573 d3	Tbx18	−2.25	1.07	0.733 (+0.184)	T-box18
57	SM2181 e5	Tcf20	−1.94	1.11	0.613 (+0.114)	transcription factor 20
58	SM2175 d6	Tmem179b	−2.57	1.10	0.334 (+0.055)	transmembrane protein 179B
59	SM2591 c1	Tmem25	−1.61	1.11	0.620 (+0.099)	transmembrane protein 25
60	SM2141 e9	Trappc9	−1.62	0.95	0.778 (+0.149)	trafficking protein particle complex 9
61	SM2587 g7	Tspan10	−2.22	1.09	0.514 (+0.035)	tetraspanin 10
62	SM2149 a4	Txlna	−1.78	1.06	0.579 (+0.021)	taxilin alpha
63	SM2579 c2	Wdr37	−1.92	1.06	0.764 (+0.122)	WD repeat domain 37

List of 63 shRNAs suppressing Nhtt150Q-EGFP aggregation without distinct alteration of Nhtt16Q-EGFP expression in neuro2a cells. Targets genes of shRNAs and data summary of 1st (z-score), 2nd (ratio to control) and 3rd screening (ratio to control ± SD) are described. In case of Pik3c2a, two different shRNAs were obtained. Clone IDs of shRNAs are originally named in this paper based on plate number and well position of the shRNA.

doi:10.1371/journal.pone.0093891.t001

We have previously performed mass spectrometry of Nhtt150Q-EGFP aggregates purified from neuro2a cells and identified several aggregate-interacting proteins such as ubiquilin-1,-2, FUS/TLS and NF-YA/-YC [5,8,46]. By re-checking the data, we noticed that Tcf20 was contained in the mass spectrometry data. In addition, we found other modifiers, Hdac5 and Arhgap24, in the data, suggesting they are also the proteins incorporated into the aggregates. Analysis of their amino acid sequences revealed that Hdac5 but not Arhgap24 is relatively Q-rich (Q compositions are 8.9% and 4.8%, respectively). We also analyzed the Q composition of rest of the modifiers, however protein significantly in Q-rich like Tcf20 or Hdac5 was not found (data not shown). Taken together, these data suggest that Tcf20 and potentially Hdac5 are the proteins directly interacting with mutant Nhtt aggregates among the identified aggregation-modifiers.

Suppression of mutant Nhtt aggregation by knocking down of Csnk1d and Pik3c2a

To identify other molecular mechanisms regulating mutant Nhtt aggregation, we focused on kinases, key regulators of intracellular signal transduction. Our screening identified several kinases as potential modifiers for mutant Nhtt aggregation (Table 1, 2). These include Csnk1d, Pik3c2a and Lrguk, whose shRNAs suppressed the aggregation, and Cmpk1, Map3k1 and Pip5k1b, whose shRNAs enhanced it. The aggregation-modifying effect of these shRNAs can be reproduced when we used our own miRNAs that bind to same region as shRNA (OBS miRNA; Figure 8A), or different region (Inv-1 or -2 miRNA; Figure 1E, 8B) supporting the validity of gene knockdown effect of these kinases on the aggregation-modification. We then focused on two kinases, Csnk1d and Pik3c2a, whose knockdown suppressed Nhtt150Q-EGFP aggregation, and confirmed significant and specific reduction of gene expressions by their miRNAs (Figure 8C). We further examined the dependency of their knockdown effect on proteasome or autophagic activity, and found that their miRNAs were still effective even in the presence MG132 or Baf A1 (Figure 8D). Taken together, these data suggest that Csnk1d and Pik3c2a are involved in the modification of mutant Nhtt aggregation through proteasome- and autophagy-independent mechanisms.

Knockdown of aggregation-modifiers did not suppress mutant Nhtt-induced cell toxicity

Finally, we examined the effect of knockdown of Tcf20, Csnk1d or Pik3c2a on cell toxicity induced by mutant Nhtt. For this purpose, we first synthesized following siRNA oligos based on the miRNA sequences used above; two for Tcf20 (OBS and Inv-1) and one for Csnk1d (Inv-1) or Pik3c2a (Inv-1). We first confirmed that transduction of these siRNA induced significant and specific reduction of their target genes compared with that of non-targeting control (NT) in neuro2a cells (Figure 9A). We then transiently overexpressed Nhtt16Q-EGFP or Nhtt150Q-EGFP in siRNA-transduced cells. After two days, the cells were incubated with pyridinium iodide (PI) to detect dead cells, and percent of PI-positive cells per GFP-positive, Nhtt expressing cells was calculated by ArrayScan. As shown in Figure 9B, overexpression of Nhtt150Q-EGFP induced ~3-fold increase in PI-positive cells compared with that of Nhtt16Q-EGFP, suggesting the induction of cell toxicity by mutant Nhtt in neuro2a cells. Notably, knockdown of Tcf20, Csnk1d or Pik3c2a did not suppress the toxicity rather enhanced it, although their knockdown seemed to be also effective, but to a lesser extent, in Nhtt16Q-EGFP-expressing cells (Figure 9B). Altogether, these data suggest that downregulation of these modifiers dose not suppress mutant Nhtt toxicity in neuro2a cells.

Discussion

In this paper, we first performed large-scale shRNA screening of modifiers for mutant Htt aggregation in mammalian cells. By

Table 2. shRNAs enhancing Nhtt150Q aggregation in neuro2a cells.

			1st (150Q)	2nd (16Q)	3rd (150Q)	
No	Clone ID	Gene	z-score	Ratio	Ratio (+ SD)	Gene Description
1	SM2592 c7	Aimp2	2.24	1.13	1.446 (+0.331)	ARS interacting multifunctional protein 2
2	SM2023 a1	Aldh3b1	2.98	1.04	1.270 (+0.158)	aldehyde dehydrogenase 3 family, member B1
3	SM2598 f6	Arhgap24	1.57	1.05	1.945 (+0.103)	Rho GTPase activating protein 24
4	SM2108 a4	C1qtnf9	5.15	1.01	1.246 (+0.311)	C1q and tumor necrosis factor related protein 9
5	SM2171 f2	Cish	2.20	1.11	1.717 (+0.647)	cytokine inducible SH2-containing protein
6	SM2563 h3	Clec4e	1.86	1.07	1.512 (+0.387)	C-type lectin domain family 4, member e
7	SM2566 f12	Cml1	1.71	1.10	1.427 (+0.170)	camello-like 1
8	SM2022 g1	Cmpk1	1.89	1.01	1.283 (+0.120)	cytidine monophosphate (UMP-CMP) kinase 1
9	SM2179 c5	Cnih2	1.63	0.98	1.905 (+0.244)	cornichon homolog 2 (Drosophila)
10	SM2570 c11	Gba	1.88	1.04	1.242 (+0.297)	glucosidase, beta, acid
11	SM2110 c2	Gm10336	2.09	1.07	1.439 (+0.055)	predicted gene 10336
12	SM2168 g12	Gnai2	2.18	1.07	1.855 (+0.408)	G protein alpha inhibiting 2
13	SM2575 d8	Gnpda1	1.74	1.14	1.559 (+0.104)	glucosamine-6-phosphate deaminase 1
14	SM2014 g8	Hdac5	3.51	1.02	1.182 (+0.162)	histone deacetylase 5
15	SM2598 a11	Krcc1	2.22	1.06	1.340 (+0.225)	lysine-rich coiled-coil 1
16	SM2021 a4	Lmln	4.98	0.93	1.398 (+0.218)	leishmanolysin-like (metallopeptidase M8 family)
17	SM2111 e11	LOC210191	2.06	1.01	1.476 (+0.136)	
18	SM2113 d11	LOC226712	2.83	1.11	1.250 (+0.188)	
19	SM2187 d12	Map3k1	1.67	0.98	1.491 (+0.280)	mitogen-activated protein kinase kinase kinase 1
20	SM2173 a12	Mark3	1.52	1.15	1.524 (+0.554)	MAP/microtubule affinity-regulating kinase 3
21	SM2577 h12	Mei1	1.97	1.15	1.278 (+0.093)	meiosis defective 1
22	SM2561 g8	Myl12b	3.45	1.03	1.850 (+0.131)	myosin, light chain 12B, regulatory
23	SM2576 e12	Myo19	1.57	1.13	1.345 (+0.124)	myosin XIX
24	SM2580 c2	Mypop	1.99	1.10	1.768 (+0.066)	Myb-related transcription factor, partner of profilin
25	SM2563 f11	P2rx7	1.60	1.05	1.357 (+0.036)	purinergic receptor P2X, ligand-gated ion channel, 7
26	SM2583 c6	Pcdhb18	1.58	1.05	1.776 (+0.165)	protocadherin beta 18
27	SM2593 d2	Pcgf3	2.47	1.06	1.307 (+0.198)	polycomb group ring finger 3
28	SM2561 h8	Pcp2	2.13	1.00	1.539 (+0.278)	Purkinje cell protein 2 (L7)
29	SM2185 f10	Pip5k1b	2.02	1.02	1.423 (+0.324)	phosphatidylinositol-4-phosphate 5-kinase, type 1 beta
30	SM2563 h5	Plp2	1.84	1.11	1.652 (+0.352)	proteolipid protein 2
31	SM2022 g10	Ptpn11	2.42	1.00	1.292 (+0.176)	protein tyrosine phosphatase, non-receptor type 11
32	SM2109 c7	Rassf4	3.49	1.08	1.382 (+0.167)	Ras association domain family member 4
33	SM2139 h11	Rnf20	2.06	1.09	1.644 (+0.143)	ring finger protein 20
34	SM2109 e10	Serpinb10	3.50	1.04	1.315 (+0.178)	serine peptidase inhibitor, clade B, member 10
35	SM2598 h10	Slain2	2.25	0.98	1.479 (+0.284)	SLAIN motif family, member 2
36	SM2583 c9	Snx10	1.83	1.10	1.691 (+0.168)	sorting nexin 10
37	SM2568 e11	Spa17	1.86	1.09	1.233 (+0.191)	sperm autoantigenic protein 17
38	SM2112 g7	Spata21	4.45	0.85	1.523 (+0.099)	spermatogenesis associated 21
39	SM2568 h10	St6galnac2	1.65	1.11	1.359 (+0.195)	ST6-N-acetylgalactosaminide alpha-2,6-sialyltransferase 2
40	SM2168 f8	Stxbp1	1.52	1.08	1.713 (+0.303)	syntaxin binding protein 1
41	SM2568 d8	Sult2a2	1.59	1.11	1.338 (+0.253)	sulfotransferase family 2A
42	SM2565 c8	Svep1	2.88	1.08	1.274 (+0.266)	sushi, EGF and pentraxin domain containing 1
43	SM2184 a10	Syk	2.91	0.95	1.844 (+0.251)	spleen tyrosine kinase
44	SM2559 f11	Syt10	1.74	1.07	1.322 (+0.248)	synaptotagmin X
45	SM2142 g10	Tbc1d10c	3.38	1.07	1.402 (+0.046)	TBC1 domain family, member 10c
46	SM2587 a10	Tmem63a	1.71	1.05	1.604 (+0.054)	transmembrane protein 63a
47	SM2565 b8	Trem1	1.95	1.06	1.419 (+0.125)	triggering receptor expressed on myeloid cells 1

Table 2. Cont.

			1st (150Q)	2nd (16Q)	3rd (150Q)	
No	Clone ID	Gene	z-score	Ratio	Ratio (+ SD)	Gene Description
48	SM2583 e7	Wdpcp	2.38	1.00	1.627 (+0.187)	WD repeat containing planar cell polarity effector

List of 48 shRNAs enhancing Nhtt150Q-EGFP aggregation without distinct alteration of Nhtt16Q-EGFP expression in neuro2a cells. Targets genes of shRNAs and data summary of 1st (z-score), 2nd (ratio to control) and 3rd screening (ratio to control ± SD) are described. Clone IDs of shRNAs are originally named in this paper based on plate number and well position of the shRNA.

doi:10.1371/journal.pone.0093891.t002

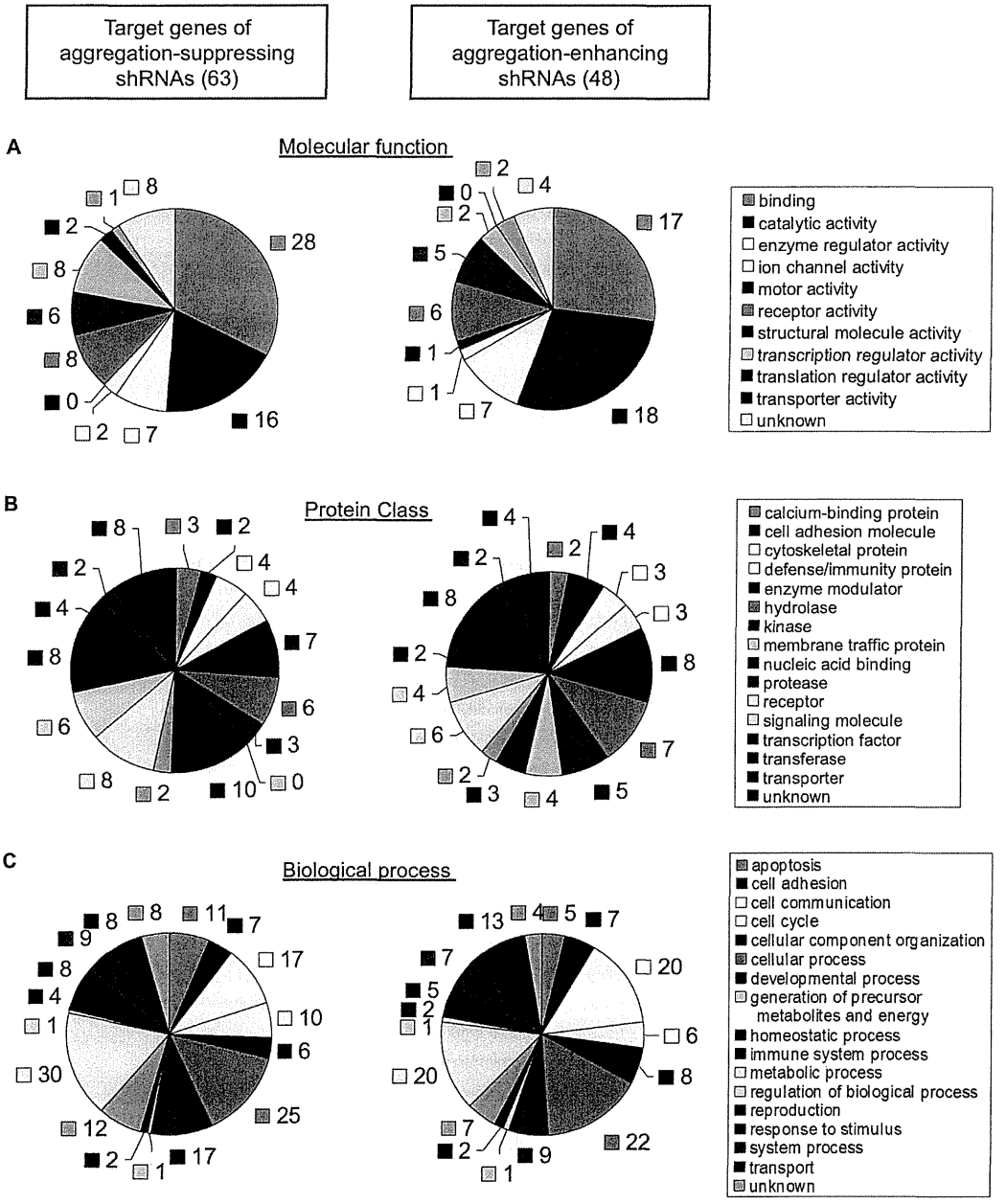

Figure 4. Classification of the shRNA-target genes. Target genes of the aggregation-suppressing (left chart) or -enhancing (right chart) shRNAs were classified using PANTHER Classification System based on molecular function (A), PANTHER Protein Class (B), or biological process (C). Genes not found in the database were classified as unknown. The numbers of classified genes were described.

doi:10.1371/journal.pone.0093891.g004

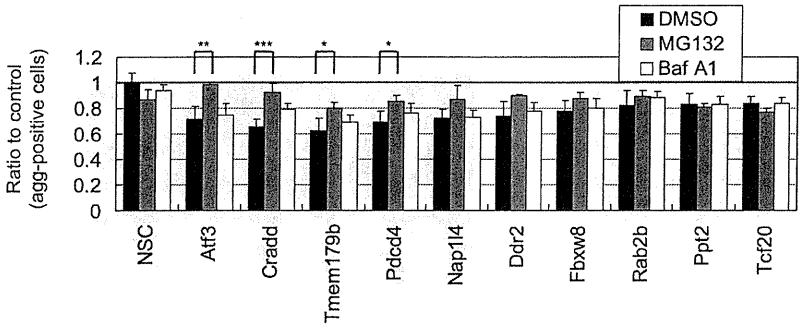

Figure 5. Effect of proteasome or autophagy inhibitor on shRNA-mediated modification of Nhtt150Q-EGFP aggregation. Nhtt150Q-EGFP cells transfected with control (NSC) or shRNAs for indicated genes were treated with 0.5 μM MG132, 0.5 μM Baf A1 or DMSO together with ponasterone A for 24 hr. The cells with Nhtt150Q-EGFP aggregates were quantified by ArrayScan reader. Some of shRNA's suppressive effects on the aggregation were relieved by treatment with MG132 but not with Baf A1. Values are means ± SD of four well data (*$P<0.05$, **$P<0.01$, ***$P<0.001$).
doi:10.1371/journal.pone.0093891.g005

transfection of neuro2a cell line expressing Nhtt with shRNA library clones and automated cell image analysis using ArrayScan HCS reader, we identified 111 shRNAs clones that specifically modified mutant Nhtt aggregation without affecting its expression in neuro2a cells. The shRNA-target genes were classified into various cellular functions including transcription and protein phosphorylation. Subsequent analysis suggests that in addition to the genes such as Atf3 whose knockdown effect was sensitive to proteasome inhibition, there were several genes whose knockdown modified the aggregation independently of it (Figure 10). These include a transcription factor Tcf20 and kinases Csnk1d and Pik3c2a. Notably, all the genes except Pik3c2a [33] are not found by the previous screenings using other organisms such as *Drosophila* and *C. elegans*. Thus, our RNAi screening using mammalian cells identified novel genes that modify mutant Htt aggregation through several, possibly mammalian-specific molecular mechanisms.

An identified modifier, Tcf20 (transcription factor 20), contains several polyQ stretches. Notably, Tcf20, as well as another relatively Q-rich modifier Hdac5 (histone deacetylase 5), was found in mutant Htt aggregates by our previous mass spectrometric analysis [46]. Indeed, we found co-localization and co-insolubilization of Tcf20 with mutant Nhtt aggregates through its N-terminal Q-rich region. In addition, anti-Tcf20 antibody stained nuclear inclusions of R6/2 mouse brain. Furthermore, overexpression of Tcf20 also modified the aggregation. These observations support the idea of physical and probably direct interaction of Tc20 with mutant Htt aggregates, which modifies the aggregation. We have previously shown that an RNA binding protein FUS/TLS, another protein identified by the mass spectrometry described above, suppresses mutant Htt aggregation [8]. In contrast, GIT1 (G protein-coupled receptor kinase-interacting protein), identified by a yeast two-hybrid screen using mutant Htt as a bait, enhances its aggregation [47]. These observations suggest that mutant Htt aggregation is differentially modulated by several interacting proteins, and Tcf20 or Hdac5 may also be the protein that directly modifies it (Figure 10). Interestingly, the modifiers identified here also include several aggregation-prone proteins such as Cradd/Raidd [48], Gpr37/Pael-R [49] and Aimp2/p38 [50]. It would be intriguing to test the co-aggregation of these with mutant Htt, which could lead to identification of another potential mechanism of direct modification of the mutant Htt aggregation.

We also found several kinases that modify the mutant Htt aggregation. One of them is Csnk1d (casein kinase 1 delta; CK1δ), a CK1 family kinase that phoshorylates many substrates with different cellular functions such as cell differentiation, proliferation, chromosome segregation and circadian rhythm [51]. Pathologically, CK1 is shown to be elevated in Alzheimer patients, and phosphorylate tau, a protein linked to Alzheimer's diseases [51]. Although the role of CK1 in polyQ diseases is unknown, overexpression of another casein kinase, CK2, is shown to reduce mutant Htt aggregates possibly through p62-madiated autophagic clearance [36]. Because we found that Csnk1d knockdown reduces the aggregates, mutant Htt aggregation may be differentially modified through these two casein kiasnes, CK1 and CK2 (Figure 10).

Another identified modifier, Pik3c2a (phosphatidylinositol 3 kinase C2 alpha; PI3K-C2α), is a class II PI3K that phosphorylates 3′ position of inositol lipids to produce mainly phosphatidylinositol 3-phosphate (PI(3)P) [52,53]. Because Pik3c2a knockdown is also shown to reduce mutant Htt aggregation in *Drosophila*, it is an evolutionally conserved modifier of the aggregation. When compared with class I conventional PI3K that produces mainly $PI(3,4,5)P_3$ [52], Pik3c2a has unique structural features, including a clathrin-binding site in the N-terminal stretch, and relative resistance to PI3K inhibitors wortmannin and LY294002 [52,54]. Although recent studies suggest its involvement in intracellular vesicular trafficking and tissue morphogenesis [54–57], the mechanism by which Pik3c2a modifies mutant Htt aggregation remains unknown. One potential pathway is through regulation of RhoA small GTPase, because Pik3c2a knockdown impaired RhoA activation in endothelial cell [57], and an inhibitor of Rho kinase, a downstream target of RhoA, suppresses mutant Htt aggregation in neuro2a cells [58]. In contrast, we found that mutant Htt aggregation was enhanced by knocking down another PI kinase, Pip5k1b, which phosphorylates 5′ position of inositol lipids to produce $PI(4,5)P_2$. Increased aggregation of mutant Htt has been also reported by suppression of a class III PI3K, Vps34, a key regulator of autophagic clearance of mutant Htt [45]. Thus, several phosphatidylinositols produced by different PI kinases may differentially modulate mutant Htt aggregation possibly through multiple molecular pathways (Figure 10).

Despite the suppression of mutant Nhtt aggregation by knocking down Tcf20, Csnk1d or Pik3c2a, we could not observe clear alteration of mutant Nhtt-induced cell toxicity by it. One possibility is that downregulation of only one gene is insufficient to alter the toxicity. Indeed, functional and/or physical interaction with polyglutamine proteins are also reported for several other shRNA target genes, such as Atf3 [59], Ddx6 [60], Fbxw8 [61], P2ry1 [62] and Map3k1 [63]. In addition, several shRNA targets